NOVEL FRONT GRID DESIGNS AND ANALYSES FOR HIGH-EFFICIENCY CRYSTALLINE SOLAR CELLS

by

Alan Rodriguez

A thesis submitted to the faculty of
The University of North Carolina at Charlotte
in partial fulfillment of the requirements
for the degree of Master of Science in
Electrical Engineering

Charlotte

2022

Approved by:

_____
Dr. Abasifreke Ebong

_____
Dr. Farid Tranjan

_____
Dr. Yong Zhang

ABSTRACT

ALAN RODRIGUEZ. Novel Front Grid Designs and analyses for high-Efficiency Crystalline Solar cells. (Under the direction of DR. ABASIFREKE EBONG)

The efficiency of a solar can be limited by reflection through both the front gridlines and non-gridline regions. In the later, poor texturing, non-optimum thickness and refractive index of the antireflection coating (ARC), could be responsible, while wide front gridlines impacts the former. By utilizing an optimized ARC on a properly textured absorbing surface, then the implementation of a narrow gridline design can curtail this unwanted optical and electrical losses. However, the implementation of narrow screen-printed gridlines is daunting, because the metal powder particle size in commercial silver paste, dictates the mesh threshold, which places an upper limit on what gridline width can be printed. Thus, an innovative "tapered finger design", where the front gridline gradually reduces in width through three stages and in turn leads to an overall low silver consumption. It is imperative that the innovative design overcomes the associated gridline and contact resistances and show an overall superior or at par performance to the conventional design. Thus, the solar cell electrical output parameters including, the fill factor, open circuit voltage, reverse saturation current and efficiency should attest to this fact.

This thesis therefore, focused on the design, modeling and fabrication of commercial size solar cells G1 CZ wafers (158mmx158mm, which was supplied from the production line after the ARC). Three front grid designs were made and converted to the printing screens (masks) including (i) a traditional front grid design with 40 μm opening, (ii) the tapered finger design (50, 40, and 30 μm opening), and (iii) the tapered finger design (50, 40, and 30 μm opening) with the addition of streets (1 mm wide). The experimental results (for the best cells), showed (i) 81.1% fill factor and 22.6% efficiency for the 40 μm opening; (ii) 79.0% fill factor and 22.0%

efficiency for the (50, 40, and 30 μm opening), and (iii) 79.2% fill factor and 21.9% efficiency for the (50, 40, and 30 μm opening with 1 mm-street width). The slight loss in performance for the innovative design could be attributed to non-optimum printing, which would require much fine tuning in particular, the squeegee pressure, the print-speed and snap-off distance to account for the difference in the design. It should be noted though that, although the 40 μm traditional gridline gave the best results, the tapered gridline with 1-mm street width is superior in the use of silver consumption by 12.5 mg. Such reduction in silver consumption would amount to a \$2M savings if this design is implemented in a Gigawatt factory.

As the PV industry is working to standardize the wafer size to G12 (210mmx210mm area) , this prompted the extension of this thesis work to include this upcoming commercial wafer size. Since the innovative design with the streets reduces the silver consumption, this design was assumed for the G12 wafer size. As at the time of this work, the G12 wafers were not available for experimental validation, thus only simulation and extrapolation of the G1 experimental results are presented here. From G1 result the silver consumption was the major advantage of the innovative design, which trend was also true for G12, showing a 59.8 mg reduction in silver consumption compared to the conventional design. This reduction in silver consumption translates to \$7M savings in a Gigawatt factory, which is very significant. Thus, the innovative design would lead to solar electricity affordability and lower LCOE.

DEDICATION

I would like to dedicate this Thesis to God, my deceased father Andres Rodriguez, my Mother Maria Piedad Arechiga, my Step-Father Alejandro Martinez, my Brothers Erick Rodriguez and Issac Martinez, and my unmentioned family for encouraging me to finish this degree. Without your spiritual, moral, emotional, and financial support this accomplishment would not have been a reality. May you continue to prevail and make the world a better place one act at a time.

ACKNOWLEDGEMENTS

First and foremost I would like to acknowledge the valuable contributions that Dr. Ebong has made to the inception of this thesis. His vast and precise knowledge of photovoltaics allowed me to pinpoint my topic and shape it into a coherent thesis. Furthermore, his spiritual guidance helped prevail through difficult chapters of my life. Secondly, I would like to acknowledge my Friends and colleagues Donald Intal and Sandra Honeycut for their consult while finishing this project.

TABLE OF CONTENTS

LIST OF TABLES

LIST OF FIGURES

LIST OF ABBREVIATIONS

FF Fill Factor

CHAPTER 1: INTRODUCTION TO PHOTOVOLTAICS

1.1 Energy and the Earth

The majority of energy present on earth originated from the sun. Of all of the energy incident upon the earth in the form of light or electromagnetic radiation, 30% (approximately 52,200 TW) is reflected back into space via cloud foliage, ocean water, ice, or the atmosphere. The remaining 70% (approximately 121,800 TW) is the available energy input into the earth [1]. There are other energy inputs into the earth such as nuclear, geothermal, and tidal flow however they make up for an extremely low amount in comparison to the sun as seen in Figure 1.1 .

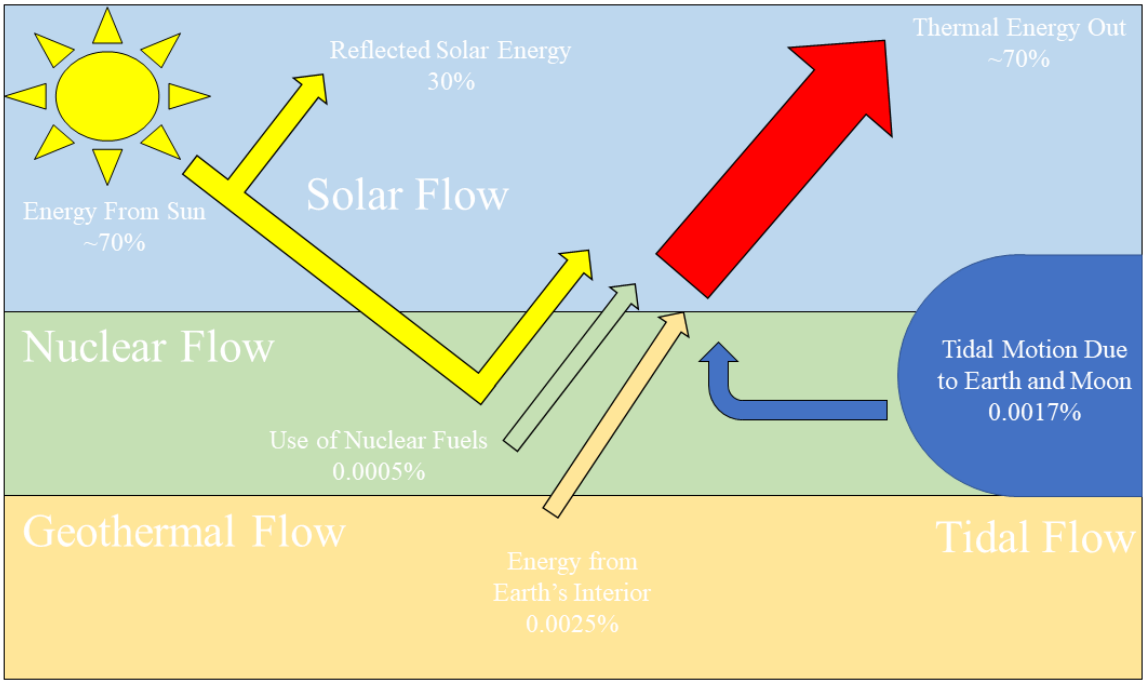

Figure 1.1: Summary of Energy Inputs Into The Earth [1]

Of the 70% energy input about 64% is consumed via the greenhouse effect [1] as seen in Figure 1.2. This is when the earth's input energy (in the form of infrared radiation) is reflected downward into the earth's surface via green house gasses present in the earth's atmosphere, which concludes in the heating of the earth [14].

From the 70% energy input about 33% is used in the hydrologic cycle [1] (also

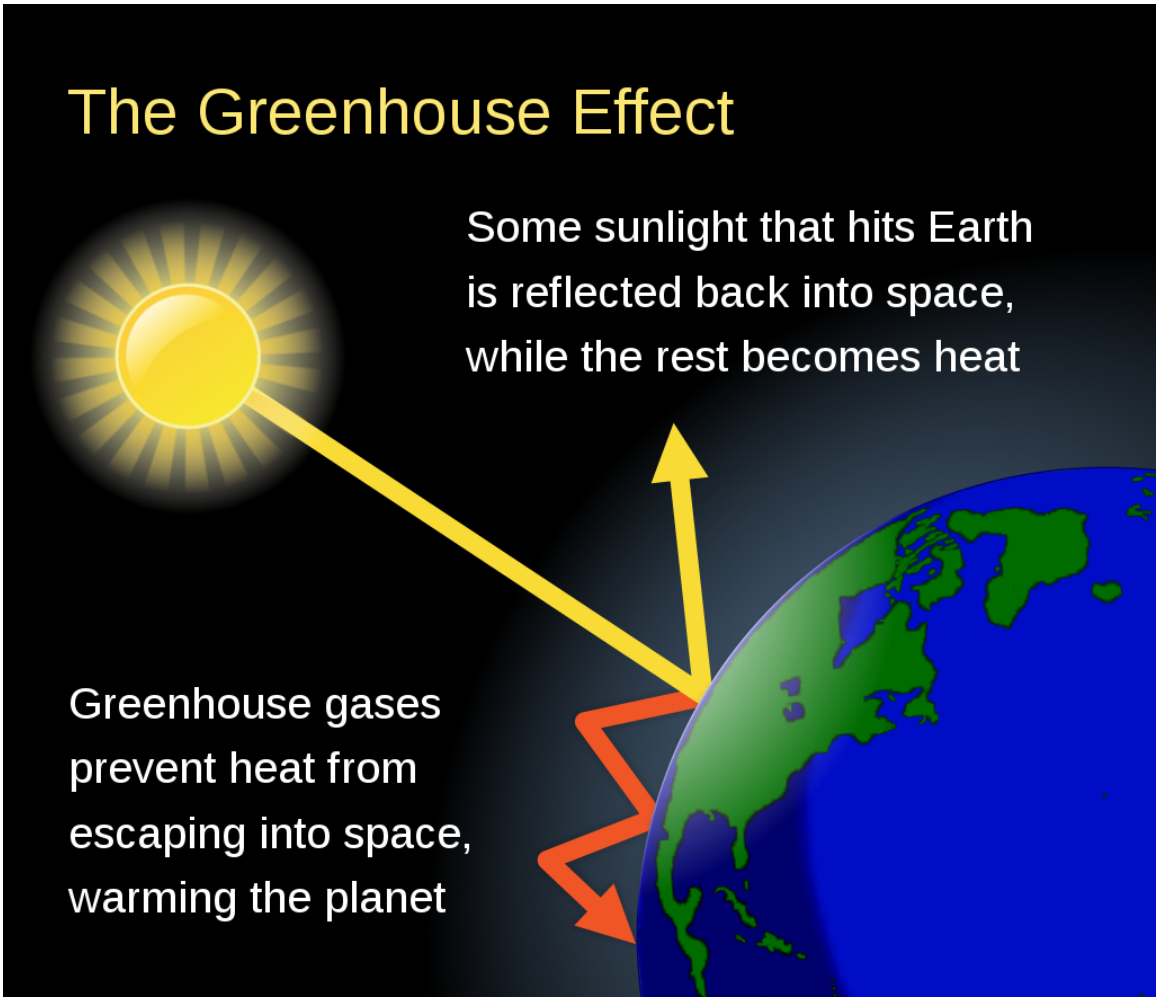

Figure 1.2: The Greenhouse Effect [2]

known as the water cycle) as seen in Figure 1.3. The hydrologic cycle begins at the heating of the oceans by the sun which results in the evaporation of water. This water travels around the earth's atmosphere as clouds which dispose of the stored water as precipitation. This precipitation can take the form of rain or snow and is responsible for the stored water on the earth's landscape. This stored water makes its way back into the oceans via rivers or precipitation and the cycle continues [3].

From the remaining energy input about 1% is dedicated to the motion of wind and water throughout the earth. This is from the kinetic energy resulting from the photon collisions on the molecules [1]

Unexpectedly, only about 0.11% of the Sun's energy input to the earth is used by

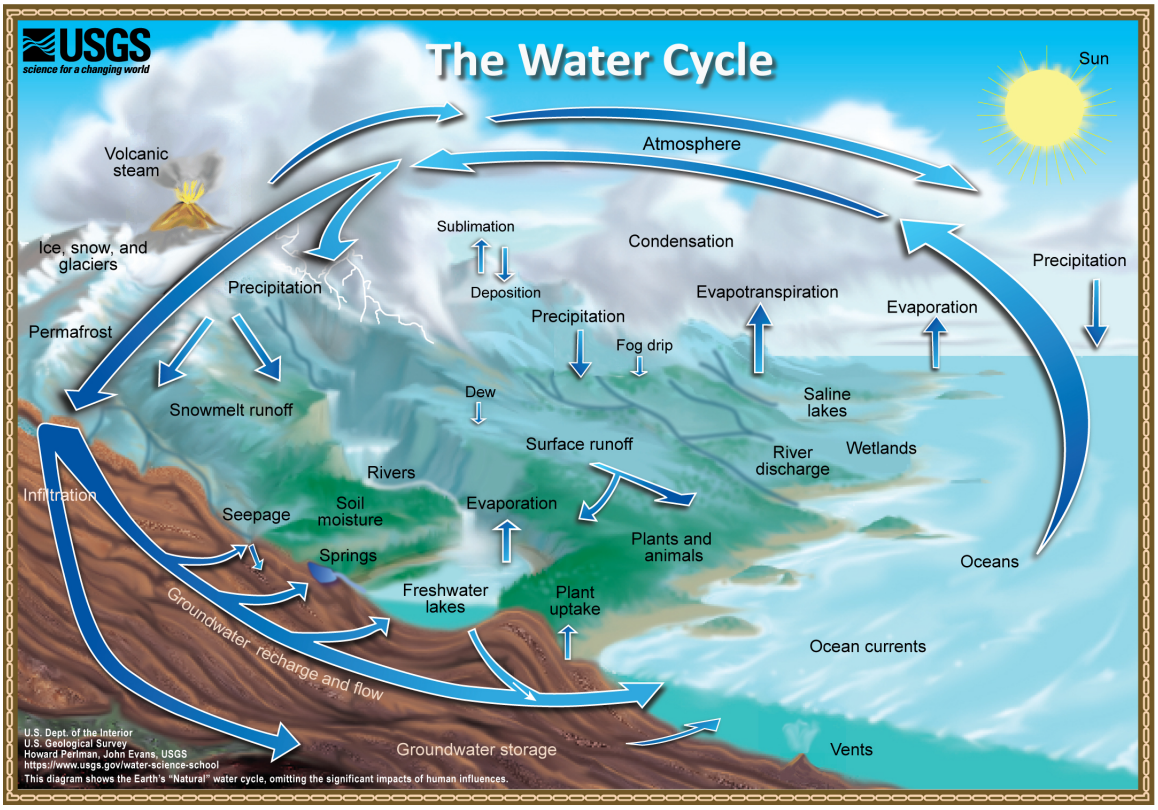

Figure 1.3: The Water Cycle [3]

plants for photosynthesis [1]. Given that plants are typically the basis of every food chain, most of the energy responsible for life on earth stems from the sun. When other species consume plants through digestion, they are breaking the chemical bonds in their molecular structure. Thus, releasing energy that is translated into movements or the essential functioning mechanisms of the consuming species.

Table 1.1 and 1.2 summarize the energy allocation of the incident energy from the sun.

Table 1.1: Summary of Incident Energy on Earth.

Percentage (%)	Incident Energy Allocation	Power (TW)
100	Total Energy Incident on the Earth	174,000
30	Energy Reflected	52,000
70	Energy Input from the sun onto the Earth	121,800

The Sun has been the Earth's main source of energy for billions of years. Life on

Table 1.2: Summary of Input Energy Allocation.

Percentage (%)	Incident Energy Allocation	Power (TW)
100	Energy Input from the sun onto the Earth	121,800
64	Greenhouse Effect	78,300
33	Hydrologic Cycle	40,00
1.4	Wind and Water Motion	1,700
0.11	Photosynthesis	140

earth has also been dependent on the Sun to thrive and evolve. It is self-evident that this must be mankind's main source of energy due to its proven consistency and sustainability to the macrobiome. This must occur not only because of its logical natural sequence, but also due to the catastrophic effects of global warming. Fossil fuels are a limited resource while the Sun's energy is essentially unlimited. To do so humanity needs a technology capable of harnessing the Sun's energy while:

- Being efficient
- Having low production costs
- Having a long lifespan
- Being sustainable

1.2 Solar Cell Energy Conversion

The main functional mechanism of a solar cell is the photoelectric effect. First discovered by German Physicist Heinrich Rudolf Hertz when he shined ultraviolet light on two metal electrodes with a voltage applied across them [15]. The light changed the voltage at which sparking also took place. This is because the incident light excited the electrons in the metal, giving them the kinetic energy to flow through the circuit. An example of this can bee seen in Figure 1.4

In the case of solar cells, the abundant expulsion of photons from the Sun is used to excite the electrons in the semiconductor body of the cell, producing the energy

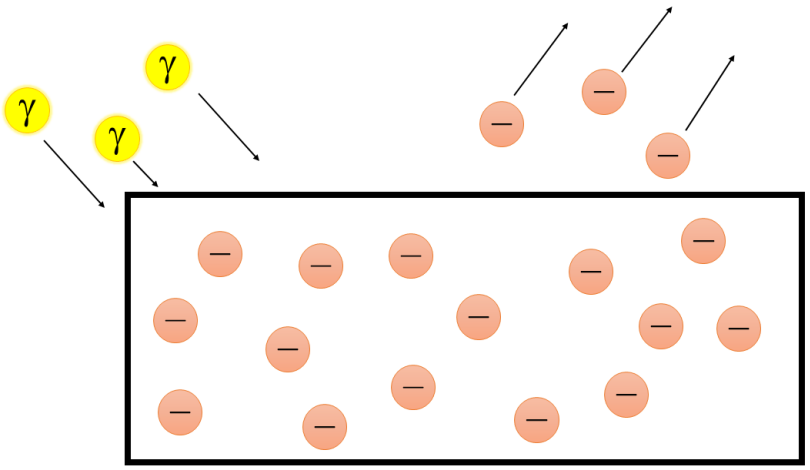

Figure 1.4: The Photoelectric Effect [4]

required to power the modern world; however, this technology is not without its drawbacks.

In order to have current flow from the solar cell into the circuit, electrons must be excited from the conduction band to the valence band as seen in Figure 1.5 . This is done via the energy from the Sun's photons.

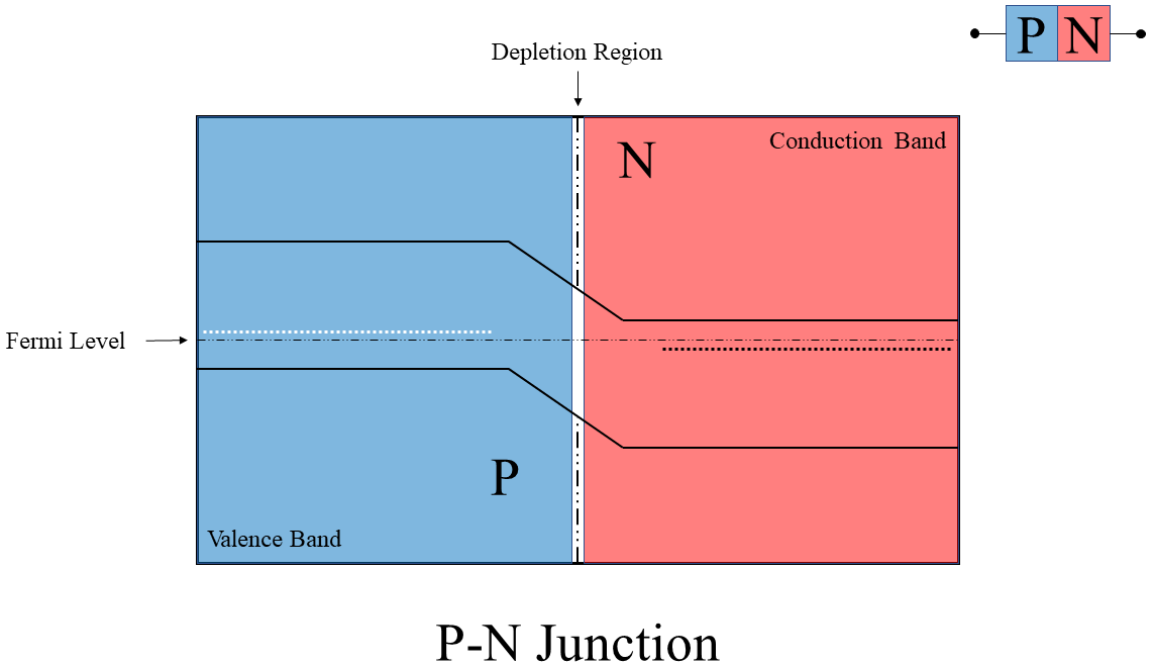

Figure 1.5: Conduction and Valence Band of a P-N Junction Semiconductor [5]

In some instances this does not happen and the photon's energy is lost. This loss

mechanism is referred to as recombination. There are various types of recombination but the three most common instances are radiative, auger, and defect assisted. as seen in Figure 1.6 .

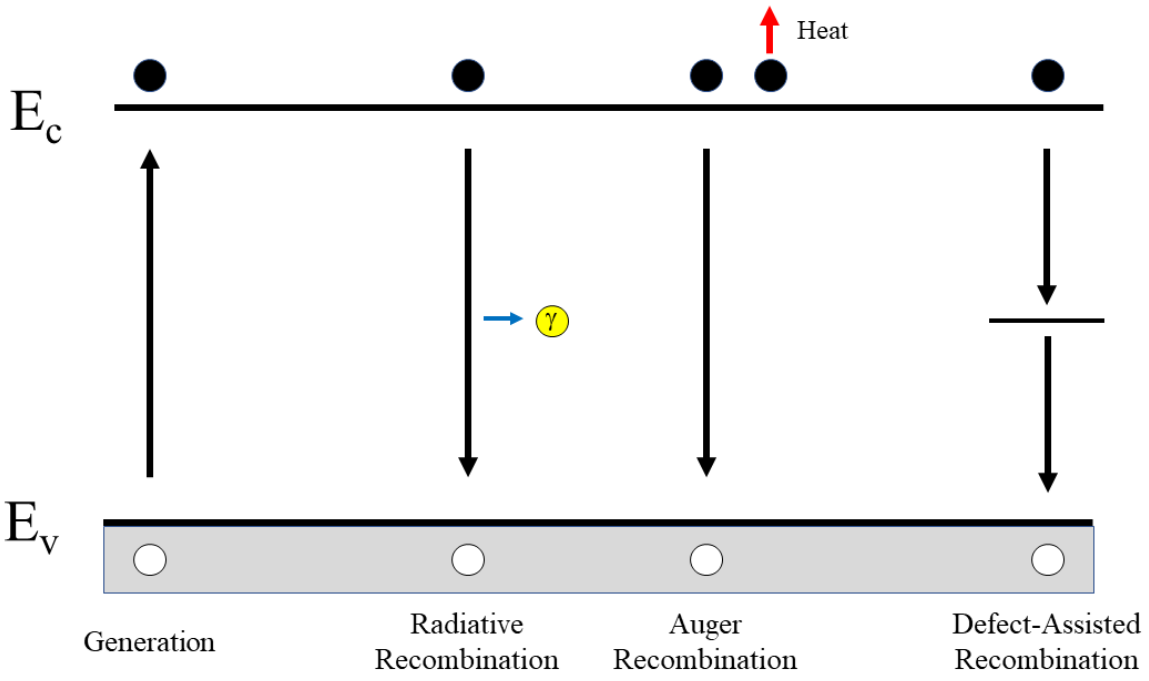

Figure 1.6: The three main recombination mechanisms [6]

Radiative recombination occurs when an electron in the conduction band degrades to the valence band by giving off its excess energy in the form of light [16]. Auger recombination occurs when an electron and hole recombine, similar to radiative recombination; however, in this instance the recombining electron gives its energy to a neighboring electron in the from of heat [16]. This electron eventually thermalizes back to equilibrium. Finally, defect-assisted recombination involves a impurity between the conduction and valence band. This causes recombining electrons to rest in the new impurity level before finally recombining to the valence band [16].

1.3 Electrical Equivalent Circuit of a Solar Cell.

$$I = I_{ph} - I_D - I_{Rsh}$$

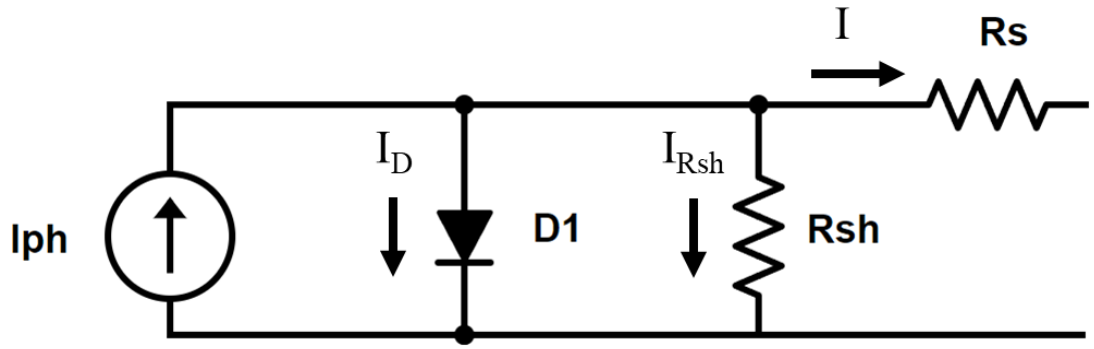

Figure 1.7: Single Diode Model of Solar Cell [7]

$$I = I_{ph} - I_s(e^{\frac{V+IR_s}{nV_T}} - 1) - \frac{V + IR_s}{R_{sh}} \tag{1.1}$$

The single diode model arises from the fundamental mechanisms of the solar cell and is mathematically described by Equation (1.1). n is the ideality factor of the solar cell under observation. V_T is simply the thermal voltage arising from the p-n junction described mathematically by $V_T = \frac{kT}{q}$. I_{ph} is the photon current originating from the sunlight incident on the solar cell. The diode in the circuit is the solar cell, which its self is simply a p-n junction device. The shunt resistance R_{sh} is derived from manufacturing defects. This loss mechanism is more prevalent at lower operating voltages, because it gives the current a less resistive path to dissipate energy which could better be utilized in the load [17]. R_s is the series resistance which is a function of three main factors [8]:

- The movement of charge carriers from the emiiter and base of the device.
- Contact resistance between the metal contacts and the Silicon.
- The top metalization pattern.

A more detailed breakdown of the series resistance arising from the top metalization patterns can bee seen in Figure 1.8.

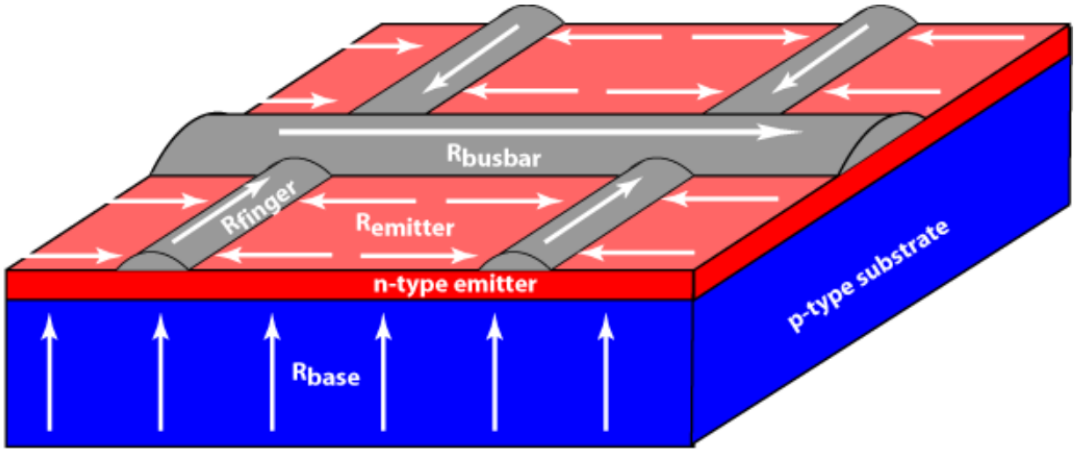

Figure 1.8: Series Resistance Arising from Top Metalization Pattern [8]

Solar cell I-V curves provide a method to extract valuable information about the device in a simple fashion. The I-V curved is derived by piloting Equation (1.1). The most notable points from this plot are the short circuit current I_{sc}, the open circuit voltage V_{oc}, and the maximum power point, denoted on the graph as P_{max}. I_{sc} is impacted by the shunt resistance while V_{oc} is influenced by the series resistance. Consequently, both the series and shunt resistance determine the maximum power point due to their relationship to I_{sc} and V_{oc} respectively.

One of the most important characteristics of an I-V curve is its ability to determine the efficiency of a solar cell. Given that I_{sc},V_{oc}, and P_{max} are know, the fill factor (FF) can be calculated as seen in Equation 1.2. The fill factor is the ratio of the area generated from the maximum power point to the area arising from I_{sc} and V_{oc}. This is best depicted in Figure 1.10.

$$FF = \frac{P_{max}}{V_{oc}I_{sc}} \tag{1.2}$$

Efficiency determines how much of the incident sunlight in converted into viable energy into the load. It should be noted that according to the Shockley-Queisser limit [18] the maximum achievable efficiency for a solar cell is 30% for the p-n junction

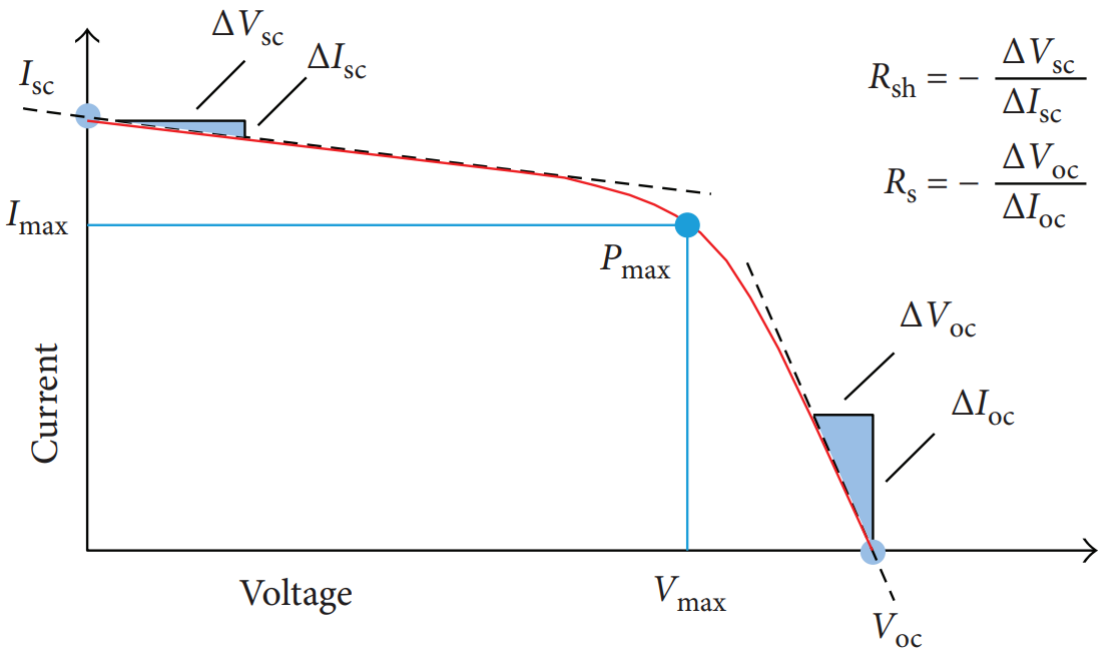

Figure 1.9: Sample I-V Curve of Solar Cell [9]

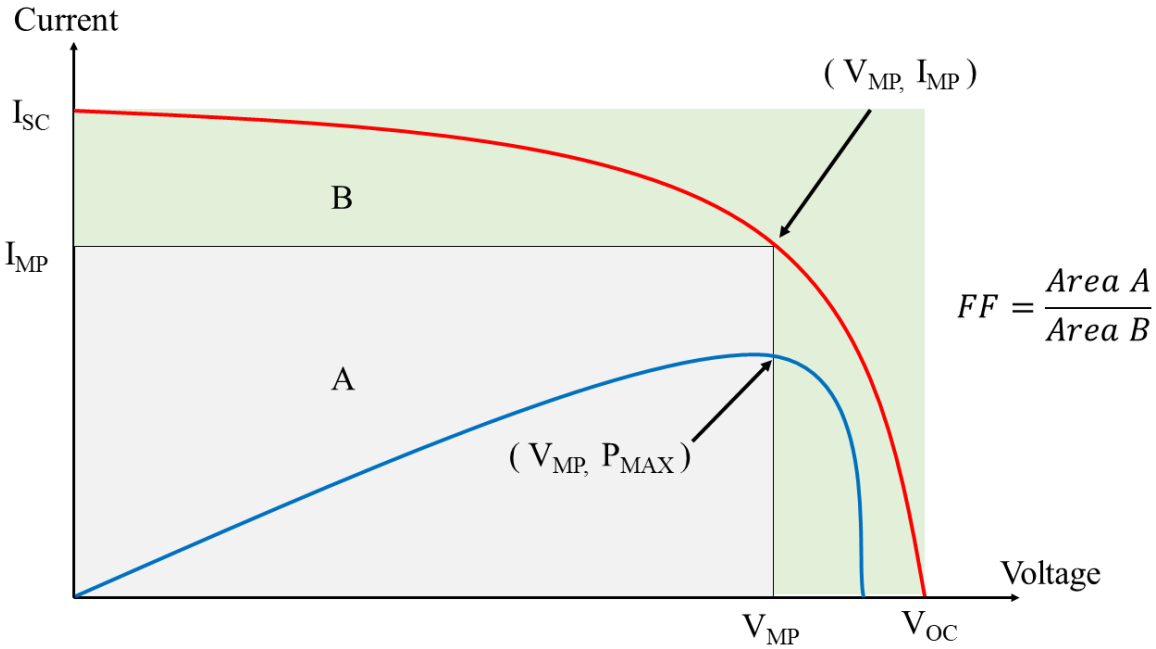

Figure 1.10: Fill Factor from I-V curve [10]

approach. The mathematical definition of solar cell efficiency can bee seen in Equation (1.3).

$$\eta = \frac{V_{oc} I_{sc} FF}{P_{in}} \tag{1.3}$$

1.4 Computational Modeling of Front Grid Designs For Series-Resistance Approximations

1.4.1 Introduction

Several grid models have been proposed and improved on, mainly by [19, 20, 21]. Thus, the methods by which the grid design impacts the series-resistance of a solar is cell is understood. The grid model implemented in the simulation of the solar cells in Chapters 2 & 3 was adopted from the works of [11]. This model was expanded to accommodate the use of streets and tapered busbars by [11]. It is highly recommended to visit his dissertation in order to have firm grasp of this model, for this section is only meant to bring light to the technique utilized in the simulation of novel grid designs.

1.4.2 Mathematical Model

The foundation of the model for streets, tapered fingers, and busbars is based on the unit cell seen in Figure 1.11. The entire solar cell is composed of iterations of this unit.

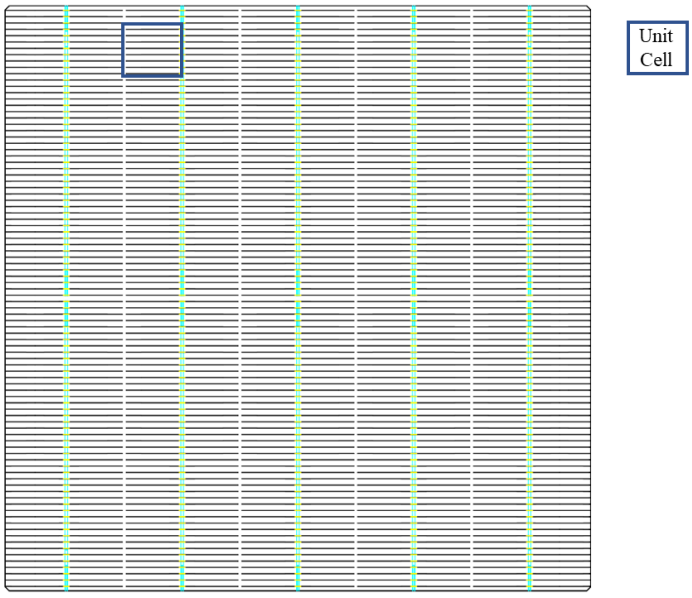

Figure 1.11: Unit Cell [11]

Table 1.3: Unit Cell Parameters

Parameter	Defenition
a	Length of Gridline
b	Half Length of Gridline Spacing
d	Half Length of Street Spacing
w	Width of Gridline
w'	Width of Busbar
n	Number of Gridlines

As seen in Figure 1.12 the dimension of this unit are $d + a + w'$ units long and $n(2b + w)$ units wide. Furthermore, a summary of the definition of each of the unit cell parameters can be found in Table 1.3

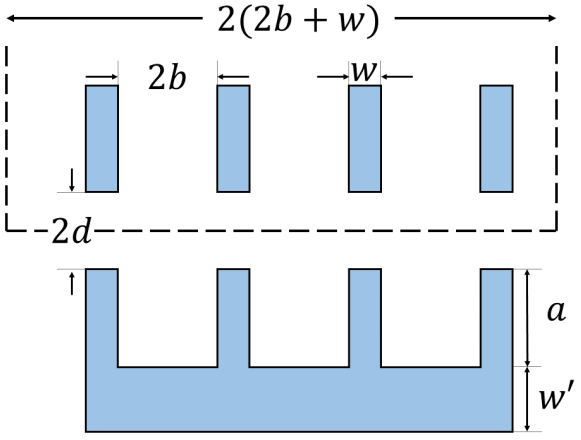

Figure 1.12: Unit Cell Dimensions [11]

Power dissipation originates from the simple equation $P = I^2\,R$. By expanding this equation to accommodate the cell's dimensional parameters, the equations often take the shape of $P = {J_L}^2\,R\,A$ or $P = {J_L}^2\,\rho\,l\,A$. In these scenarios A is an area, ρ is some resistivity, and l is some length. After evaluating the dimensions of the equations, one can make a facile deduction that they all reduce to $P = I^2\,R$; however, these expansions allow for valuable information to be extracted about each of the cell's components. This is the case for Equations (1.4),(1.6),(1.7), and (1.8) that describe the power dissipation of the emitter. R_{sheet} is the sheet resistance of the solar cell

and J_L is the current density flowing through the cell.

$$P_{Emitter1} = \frac{{J_L}^2 \, R_{\text{sheet}} \, b^3 \, \left(a - \frac{w}{2}\right)}{3} \tag{1.4}$$

$$f = \frac{11 \, \mathrm{e}^{\frac{w}{2\,d+w}}}{25} + \frac{61}{1000} \tag{1.5}$$

$$P_{Emitter2} = \frac{2 \, {J_L}^2 \, R_{\text{sheet}} \, (b-d)^3 \, (2\,d+w)}{3} + \frac{{J_L}^2 \, R_{\text{sheet}} \, (2\,d+w)^4}{2\,\pi} \left(\frac{f \, (2\,b-2\,d)}{2\,d+w} + 1\right) \left(\ln\left(\frac{2\,d+w}{w}\right) + \frac{w^2}{(2\,d+w)^2} - \frac{w^4}{4\,(2\,d+w)^4} - \frac{3}{4}\right) \tag{1.6}$$

$$P_{Emitter2'} = -\frac{2 \, {J_L}^2 \, R_{\text{sheet}} \, (b-d)^3 \, (2\,b+w)}{3} - \frac{{J_L}^2 \, R_{\text{sheet}} \, (2\,b+w)^4}{2\,\pi} \left(\frac{f \, (2\,b-2\,d)}{2\,b+w} - 1\right) \left(\ln\left(\frac{2\,b+w}{w}\right) + \frac{w^2}{(2\,b+w)^2} - \frac{w^4}{4\,(2\,b+w)^4} - \frac{3}{4}\right) \tag{1.7}$$

$$P_{Emitter} = \begin{cases} P_{Emitter} = 2\,n\,(P_{Emitter1} + \frac{P_{Emitter2}}{4}), \text{ if } b \geq d \\ P_{Emitter} = 2\,n\,(P_{Emitter1} + \frac{P_{Emitter2'}}{4}), \text{ if } b \leq d \end{cases} \tag{1.8}$$

L_T is the transfer length of the contacts and ρ_c is the resistivity of the contacts.

$$L_T = \sqrt{\frac{\rho_c}{R_{sheet}}} \tag{1.9}$$

$$P_{Contact} = \frac{4 \, {J_L}^2 \, L_T \, R_{\text{sheet}} \, n \coth\left(\frac{w}{L_T}\right) \, \left(a\,b + d\,\left(b + \frac{w}{2}\right)\right)^2}{a} \tag{1.10}$$

The power dissipation of the gridlines arises from the adoption of the Gaussian structure gridline [21], which results in the scaling factor q. Furthermore, H_f is the height of the gridline and ρ_f is the resistivity of the gridline.

$$q = \frac{10141204801825835211973625643008}{602064273162291996388051177157 7} \approx 1.6844$$

$$P_{gridline} = \frac{q\, {J_L}^2\, n\, \rho_f\, \left(\frac{4\, a^3\, b^2}{3} + a\, d^2\, (2\, b + w)^2 + 2\, a^2\, b\, d\, (2\, b + w)\right)}{H_f\, w} \tag{1.11}$$

Equation (1.12) describes the power dissipation for even busbars, where H_b is the height of the busbar; however, for the uneven case Equation (1.13) is the suitable description of power dissipation. Here w_1 is the width of the major part, w_2 is the width of the minor part, and s is the ratio of major part length to total busbar length.

$$P_{busbar} = \frac{{J_L}^2\, n^3\, \rho_f\, \left(b + \frac{w}{2}\right)^3 \left(a + d - \frac{a\, w}{2\, b + w}\right)^2}{3\, H_b\, w'} \tag{1.12}$$

$$P_{busbarUE} = -\frac{{J_L}^2\, n^3\, \rho_f\, \left(\frac{(s-1)^3}{w_2} - \frac{(s-1)^3+1}{w_1}\right) \left(b + \frac{w}{2}\right)^3 \left(a + d - \frac{a\, w}{2\, b + w}\right)^2}{3\, H_b} \tag{1.13}$$

For the base power dissipation ρ_w is the resistivity of the base and t_w is the thickness of the base.

$$P_{base} = \frac{4\, {J_L}^2\, n\, \rho_w\, t_w\, \left(a\, b + d\, \left(b + \frac{w}{2}\right)\right)^2}{(2\, b + w)\, (a + d + w')} \tag{1.14}$$

In order to normalize the power dissipation to a unit cell, the summation of all power components is divided by the normalization factor N_f in Equation (1.15) which is the unit cell area. Doing so concludes to the power dissipation of the series resistance

P_{Rs} in Equation (1.16).

$$N_f = n\,(2\,b + w)\,(d + a + w') \tag{1.15}$$

$$P_{Rs} = \frac{P_{Emitter} + P_{Contact} + P_{gridline} + P_{busbar} + P_{base}}{N_f} \tag{1.16}$$

Finally, one can arrive at the normalized series resistance R_s $(\Omega - cm^2)$ in Equation (1.17) by deviding by ${J_L}^2$

$$R_s = \frac{P_{Rs}}{{J_L}^2} \tag{1.17}$$

1.4.3 Implementation and Application

In order to utilize the aforementioned equations, they were implemented into the MATLAB software. MATLAB allows for facile manipulation of these equations by inputting them into functions, which automate the calculation process of power dissipation. Moreover, beautiful and legible graphs can be generated with this software; however, MATLAB will not suffice in deducing more specific solar cell parameters, such as efficiency for solar cells with these novel front grid designs. To solve this issue, the series resistance measurements from MATLAB will be input into the PC1D simulation software. PC1D is widely accepted in the photovoltaics community for its simplicity and transparency. The marriage between these two programs will allow for the accurate simulation and comparison to experimental results of novel front grid designs.

CHAPTER 2: NOVEL FRONT METALIZATION PATTERNS ON G1 CELLS

2.1 Introduction

The photovoltaic community has made tremendous strides since the inception of the first solar cell in 1883. The days of low efficiency and high cost are slowly fading. Clever fabrication methods and selection of materials have made this a reality; however, front grid designs are just as important and a simple method to contribute to the innovative nature of solar cell design. Some primitive front grid designs encompass a single busbar with $\approx 100\mu$m finger width as seen in Figure 2.1.

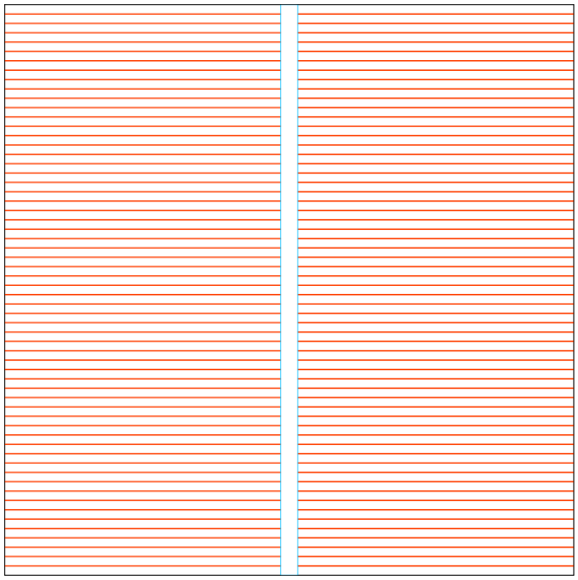

Figure 2.1: Simple solar cell design

At first glance one can conclude that these designs suffered heavily from low fill factor, primarily due to the power loss from shadowing. This is because choosing between high metalization for low resistance and low metalization for high fill factor is a hard bargain. On one hand it is beneficial to use more metal to decrease the series resistance , but this comes at the cost of more of the emitter being deprived of incident photons. Luckily, thoughtful designs such as seen in Figure 2.2 attempt to address these constraints by lowering the amount of front metal used while maintaining or increasing the fill factor

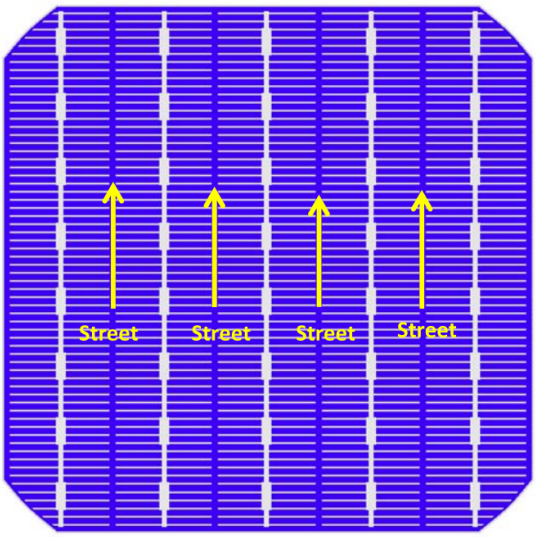

Figure 2.2: 4 Street 5 Busbar design [12]

The innovation proposed in this thesis wishes to expand on [12] by coupling the tapered finger design with 4S-5BB and analyzing the impacts of it on fill factor, efficiency, and series resistance. The tapered finger design as seen in Figure 2.3 decreases the power losses due to shadowing by decreasing the area covered by the gridlines. As the gridline approaches the other busbar it decreases in width twice. This results in a fraction of the typical power loss due to shadowing in traditional designs. Furthermore, this design maintains a high fill factor and efficiency while consuming less silver.

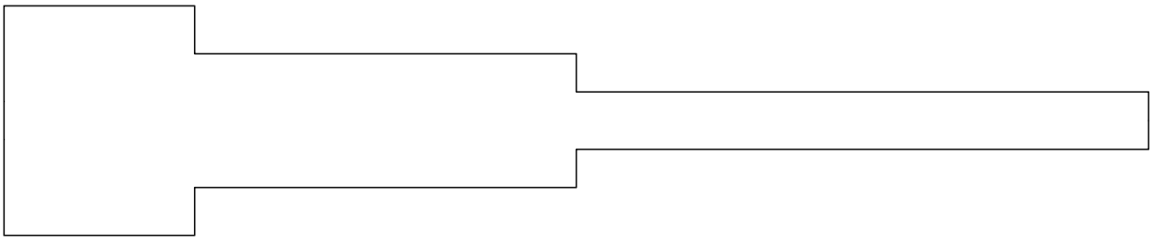

Figure 2.3: Tapered Finger Design

2.2 Experimental Procedure

To achieve the aforementioned aim of this thesis, screen designs must be produced in such a way to encompass the novel grid designs. This is easily accomplished through the use of the AutoCAD design software. This software allows for the detailed inception of line patterns, which proves beneficial in solar cell design. Through the use of AutoCAD, three screen design were made and their specification summarized in Table 2.1 and seen in Figures 2.4, 2.6, and 2.8.

Table 2.1: Summary of Experimental Solar Cell Parameters.

Cell Parameter	Cell A	Cell B	Cell C
Finger Width	40 μm	50 μm,40μm,30μm	50 μm,40μm,30μm
Number of Streets	0	0	4

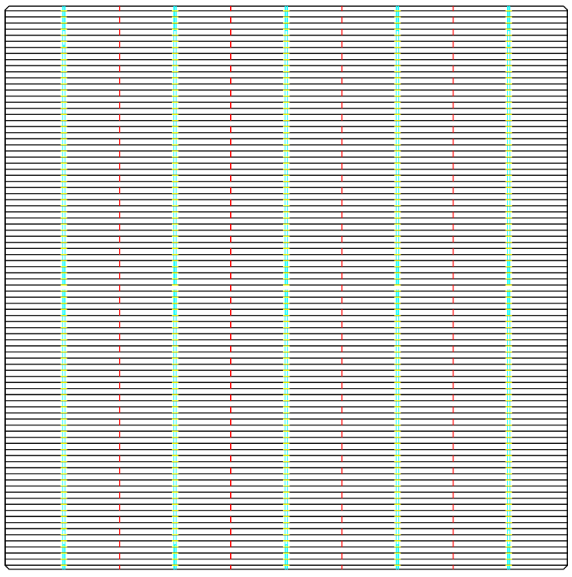

Figure 2.4: Cell A

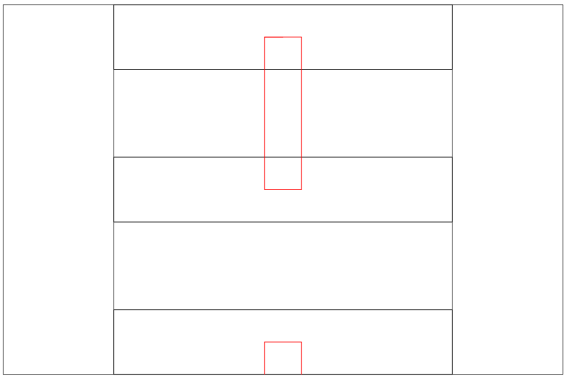

Figure 2.5: Cell A Zoom

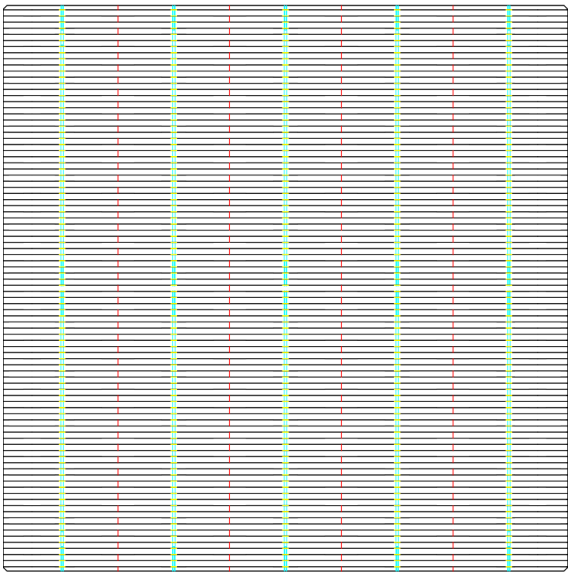

Figure 2.6: Cell B

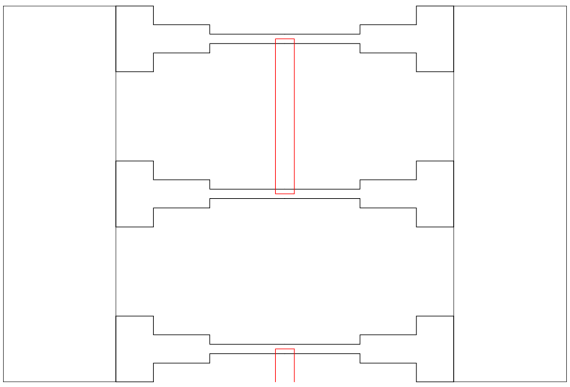

Figure 2.7: Cell B Zoom

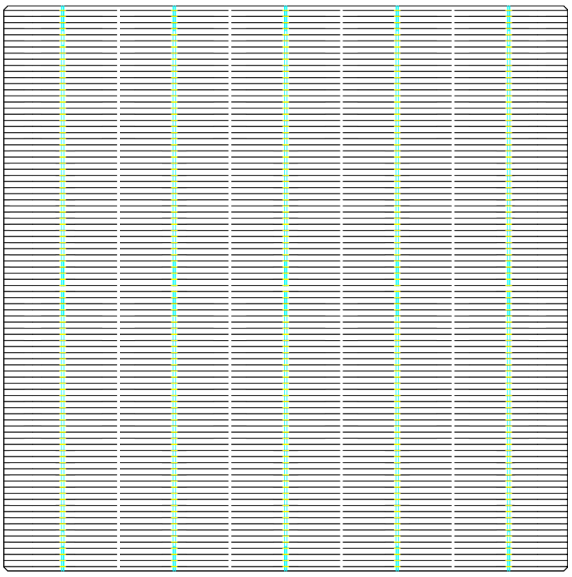

Figure 2.8: Cell C

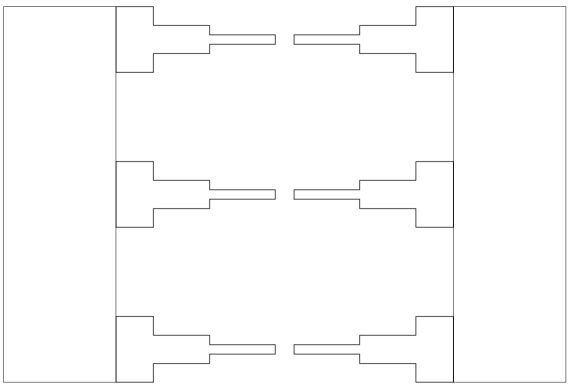

Figure 2.9: Cell C Zoom

Cell A is the control group of the experiment, for it is contains a traditional front grid design found in industry. Cell B and C are the experimental group and aim to find the advantages of the new screen design. All of the cells were printed using the EKRA screen printer, dried using the TP solar dryer, and fired through the TP solar annealing furnace. After a successful printing session, the cells were placed in the IV tester in order to determine their characterization parameters. The experimental

procedure is best depicted by Figure 2.10.

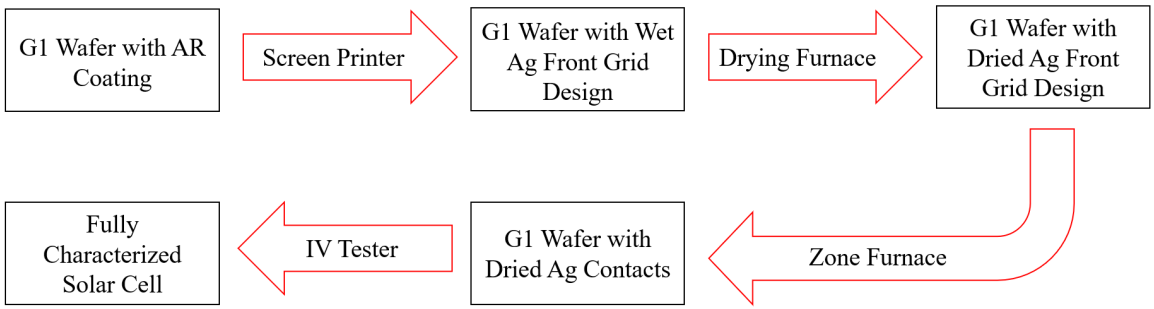

Figure 2.10: Solar Cell Fabrication Procedure

2.3 Results

First and foremost, the width of the gridlines were measured to ensure the printing screen produced the right dimensions onto the wafer. Looking at Figure 2.11, one can easily note the transition between the $50\mu m$ and the $40\mu m$ tapering.

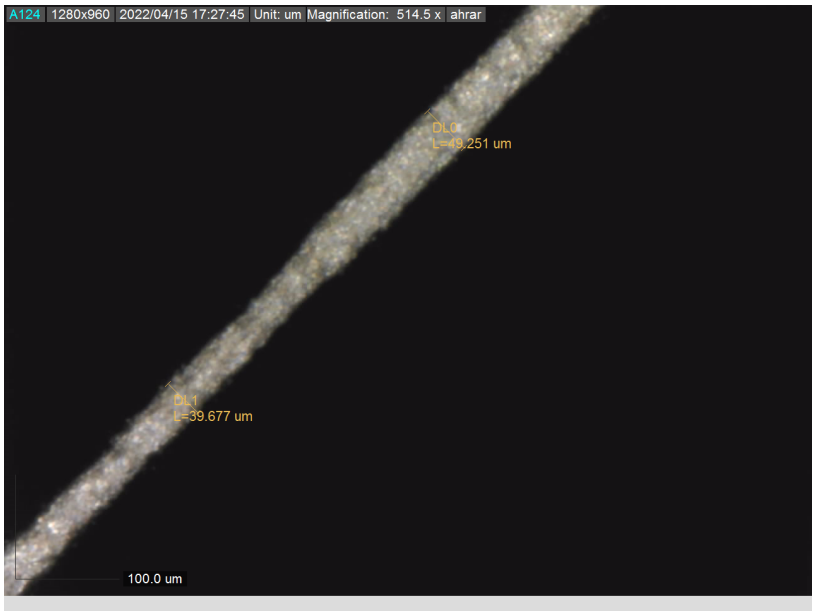

Figure 2.11: Transition between $50\mu m$ and $40\mu m$

Looking at Figure 2.12 the transition is not so clear. This could be due to the large metal particle size inhibiting a print that well defines the tapered design. Furthermore, such defects could be attributed to a larger series resistance, which would degrade the fill factor of the cell.

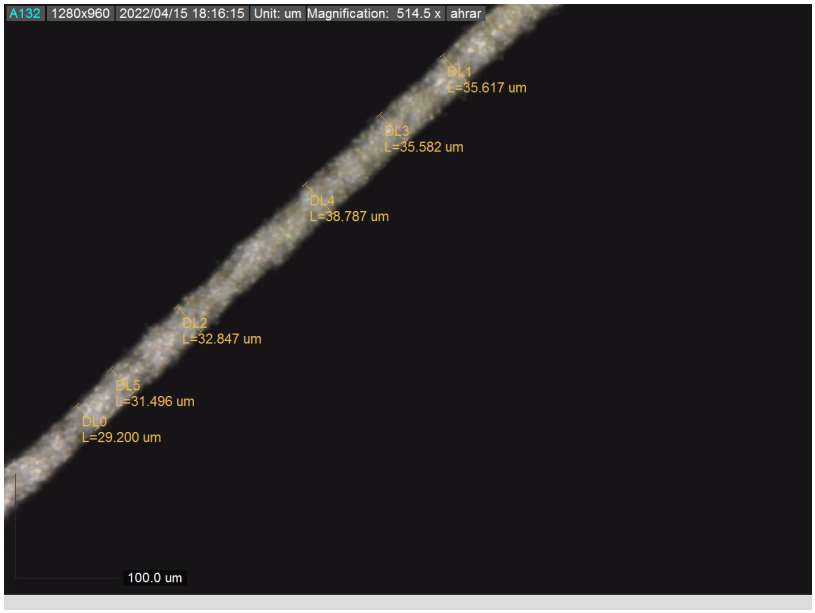

Figure 2.12: Transition between $40\mu m$ and $30\mu m$

Table 2.2: Summary of Series Resistance Results

Cell ID	Series Resistance $(\Omega - cm^2)$		
	Cell A	Cell B	Cell C
1	0.538	0.798	1.310
2	0.932	0.792	0.916
3	0.684	1.054	0.910
4	0.719	1.113	1.044
5	0.540	0.821	0.911
6	0.366	0.792	1.568
7	0.555	0.826	0.701
8	0.590	0.930	0.999
9	0.492	0.662	0.985
10	0.521	0.778	0.872
Average	**0.594**	**0.857**	**1.021**
Theoretical	**0.589**	**0.841**	**1.090**
% Error	**0.820**	**1.850**	**6.240**
Average ΔR_s	**0.501**	**0.263**	**0.165**

As mentioned in Section 1.4 of the introduction, the mathematical model devised by [11] was implemented into MATLAB. This model was used in this experiment to simulate the effects of novel front grid designs on the series resistance of solar cells. Furthermore, this experiment will help validate the mathematical model. On the same

note, Table 2.2 summarizes the experimental series resistance results, which closely matched the theoretical calculations. Figures 2.13, 2.14, and 2.15 depict graphical distribution of the data. the increasing value of series resistance is due to the narrowing gridlines and decreased consumption of Silver.

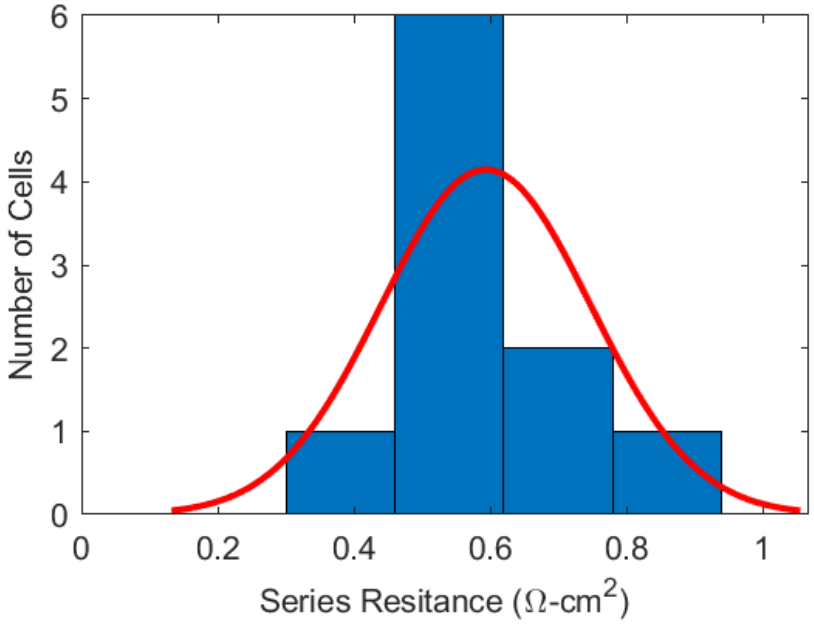

Figure 2.13: Series Resistance Distribution of Cell A

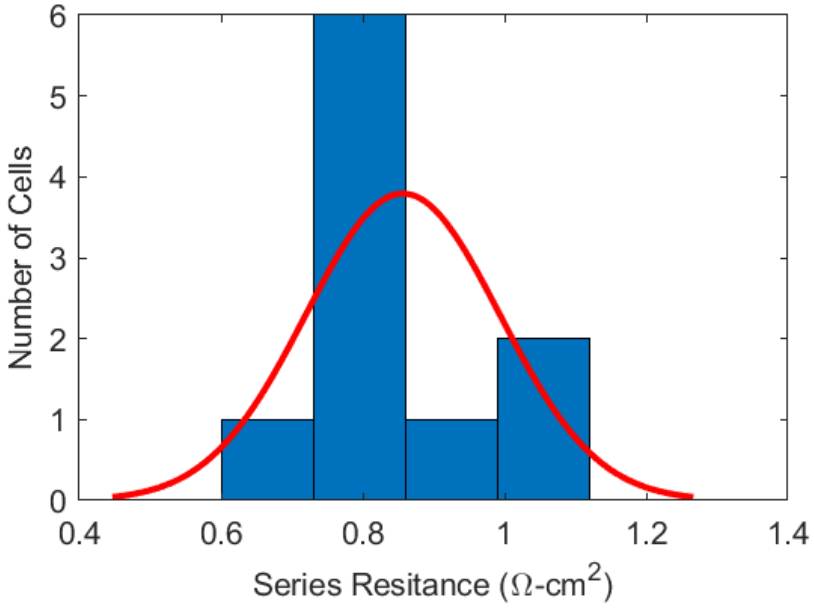

Figure 2.14: Series Resistance Distribution of Cell B

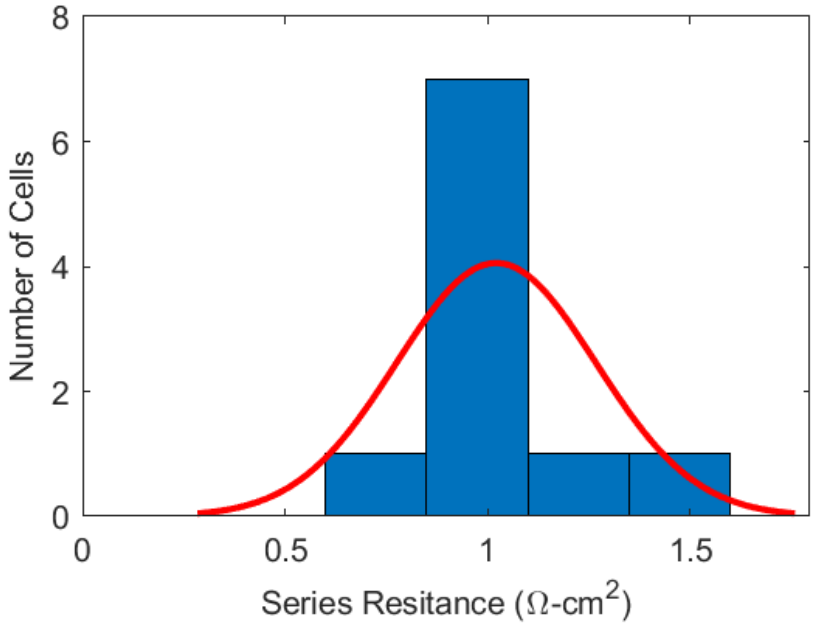

Figure 2.15: Series Resistance Distribution of Cell C

As can be seen, the data fit a normal distribution with most of the data points falling with the theoretically calculated values.

Table 2.3: Summary of Cell A's Experimental Results

Cell ID	$V_{oc}(mV)$	$J_{sc}(\frac{mA}{cm^2})$	FF (%)	Efficiency (%)	n-factor
CA1	670	41.49	80.45	22.39	1.001
CA2	673	41.77	78.24	21.99	0.992
CA3	674	41.82	79.62	22.46	0.983
CA4	674	41.72	79.29	22.31	0.986
CA5	670	41.49	80.58	22.42	1.001
CA6	**669**	**41.56**	**81.10**	**22.56**	**1.004**
CA7	669	41.55	79.95	22.22	1.006
CA8	672	41.65	80.00	22.41	1.000
CA9	670	41.51	80.53	22.41	1.007
CA10	671	41.57	80.32	22.42	1.005
Average	**671**	**41.61**	**80.01**	**22.36**	**0.999**
Theoretical	**676**	**39.90**	**79.93**	**21.55**	
% Error	**0.67**	**4.29**	**0.10**	**3.75**	

The experimental results for the performance parameters of Cell A seen in Table 2.3 closely matched the theoretical calculations. CA6 was the distinguished cell from the batch, reaching a fill factor of %81.10 and an efficiency of %22.56. Being the

industry standard, the process for making cells with this front grid design has been perfected, which allows for such favorable results to be achieved. Furthermore, the graphical distribution of Cell A's fill factor and efficiency data can be see in Figures 2.16 and 2.17 respectively.

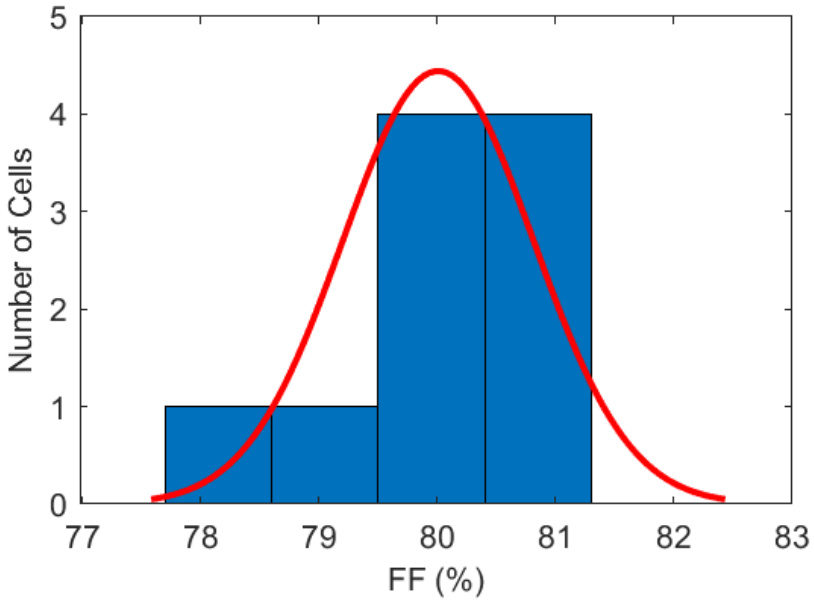

Figure 2.16: Fill Factor Distribution of Cell A

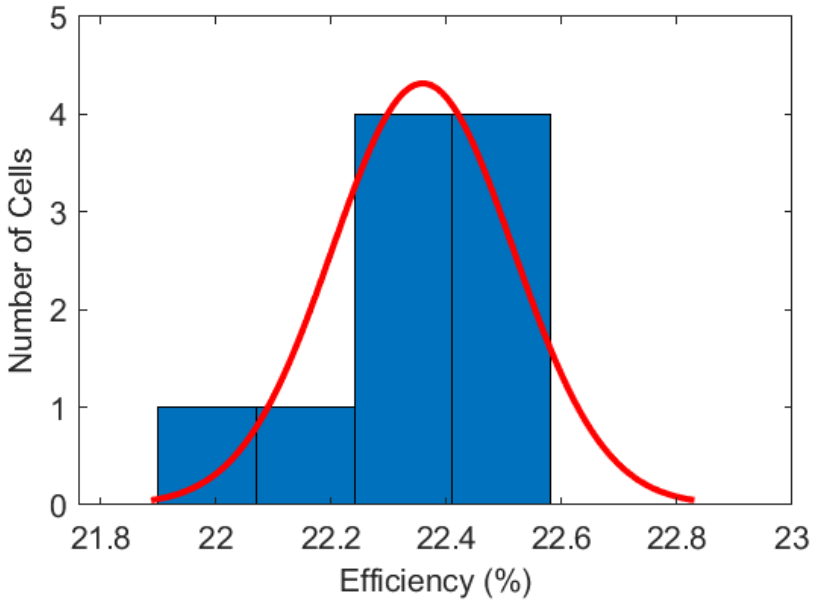

Figure 2.17: Efficiency Distribution of Cell A

The experimental results for the performance parameters of Cell B seen in Table 2.4

closely matched the theoretical calculations. CB2 was the best cell from the batch, reaching a fill factor of %79.02 and an efficiency of %21.95. As mentioned earlier, the defects found in the measurements of the gridline can be attributed the lower fill factor and efficiency. The graphical distribution of Cell A's fill factor and efficiency data can be see in Figures 2.18 and 2.19 respectively.

Table 2.4: Summary of Cell B's Experimental Results

Cell ID	$V_{oc}(mV)$	$J_{sc}(\frac{mA}{cm^2})$	FF (%)	Efficiency (%)	n-factor
CB1	663	41.34	78.64	21.55	1.020
CB2	**668**	**41.60**	**79.02**	**21.95**	**0.995**
CB3	667	41.78	77.07	21.48	1.013
CB4	667	41.39	76.72	21.16	1.013
CB5	668	41.76	78.58	21.92	1.004
CB6	665	41.33	78.15	21.47	1.035
CB7	665	41.60	78.44	21.70	1.014
CB8	665	41.55	78.11	21.62	0.996
CB9	663	41.35	79.47	21.80	1.011
CB10	663	41.36	78.70	21.60	1.011
Average	**665**	**41.51**	**78.30**	**21.63**	**1.011**
Theoretical	**676**	**39.90**	**78.52**	**21.18**	
% Error	**1.57**	**4.03**	**0.3**	**2.10**	

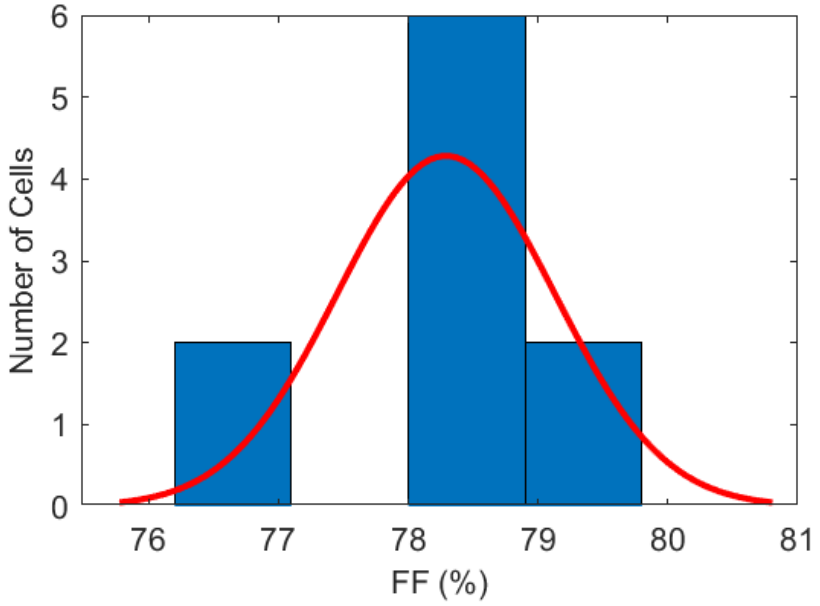

Figure 2.18: Fill Factor Distribution of Cell B

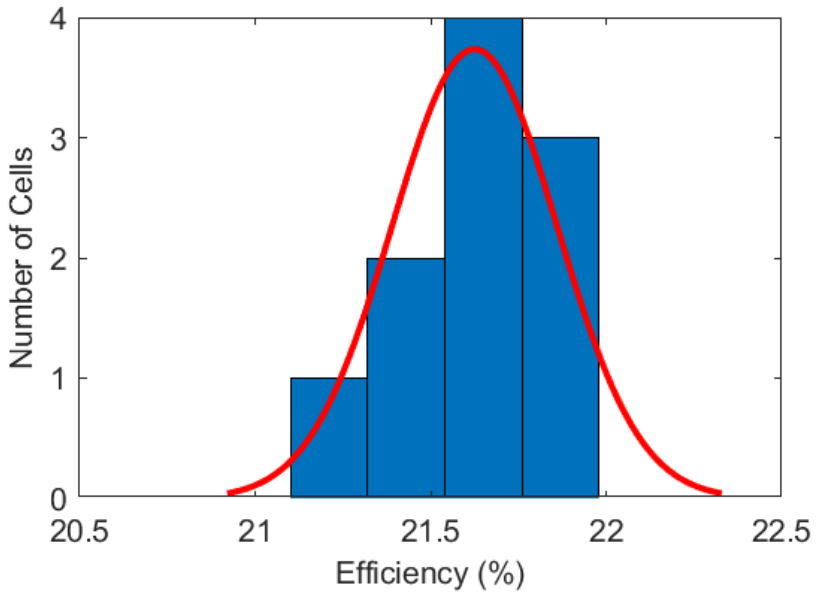

Figure 2.19: Efficiency Distribution of Cell B

The experimental results for the performance parameters of Cell C seen in Table 2.5 closely matched the theoretical calculations. CC7 was the best cell from the batch, reaching a fill factor of %79.16 and an efficiency of %21.91. The addition of streets further increased the series resistance of cell, which can be attributed to the lower fill factor and efficiency . The graphical distribution of Cell A's fill factor and efficiency data can be see in Figures 2.20 and 2.21 respectively.

Table 2.5: Summary of Cell C's Experimental Results

Cell ID	$V_{oc}(mV)$	$J_{sc}(\frac{mA}{cm^2})$	FF (%)	Efficiency (%)	n-factor
CC1	667	41.87	75.94	21.22	0.987
CC2	663	41.54	77.79	21.45	1.025
CC3	667	41.67	77.94	21.68	1.017
CC4	664	41.58	77.47	21.38	0.991
CC5	664	41.62	78.40	21.66	0.983
CC6	665	41.60	73.32	20.30	1.006
CC7	**665**	**41.61**	**79.16**	**21.91**	**1.000**
CC8	667	41.74	77.55	21.59	0.999
CC9	668	41.87	77.59	21.70	0.998
CC10	665	41.52	77.92	21.51	1.037
Average	**665**	**41.66**	**77.31**	**21.44**	**1.004**
Theoretical	**676**	**39.90**	**77.19**	**20.82**	
% Error	**1.55**	**4.42**	**0.15**	**2.98**	

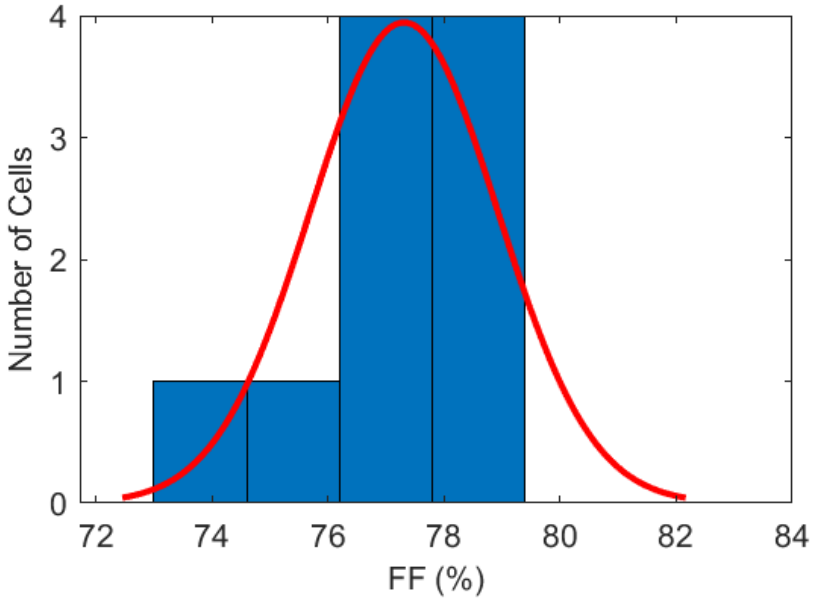

Figure 2.20: Fill Factor Distribution of Cell C

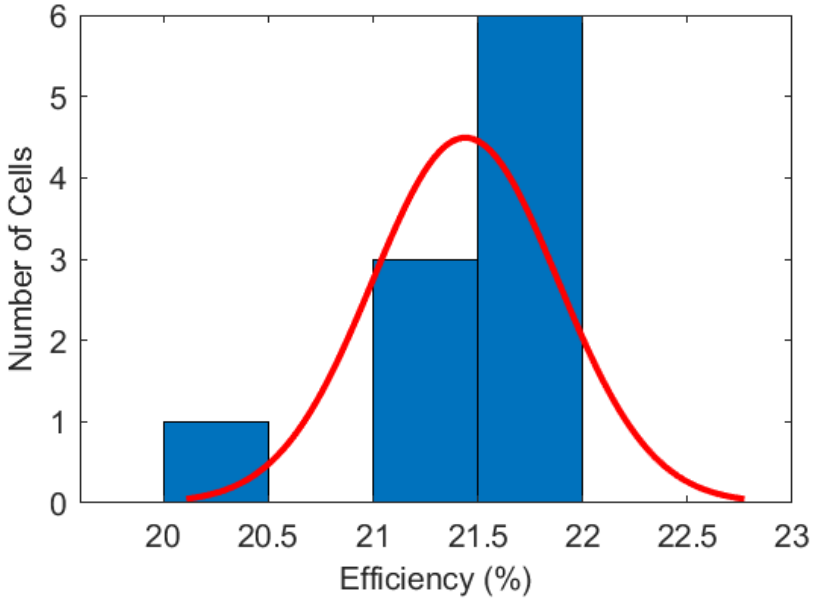

Figure 2.21: Efficiency Distribution of Cell C

2.4 Monetary Impact

The price of Silver was indexed [22] (04/17/2021) to asses the monetary impact of the tested front grid designs and justify their advantages. The price of the Silver consumption was divided by their power output in order to arrive at the metalization

cost per Watt ($\frac{¢}{W}$) figure. The results of this analysis can be seen in Table 2.6

Table 2.6: Silver Consumption Summary

04/17/2022 [22] Cost of Silver ($\frac{\$}{Kg}$)			825.00
Power Output of G1 Cell (W)			5.2
Reference Cell Weight (g)			9.7800
	Cell A	Cell B	Cell C
Weight (g)	9.8500	9.8455	9.8375
Silver Consumption (mg)	70	65.5	57.5
Silver Cost (¢)	5.78	5.40	4.74
Metalization Cost per Watt ($\frac{¢}{W}$)	1.111	1.039	0.912

The metalization cost per Watt was scaled to fit the demands of a Gigawatt factory in Table 2.7. It is here where the novel front grid designs flaunt their advantage. By simply implementing Cell C's design, a Gigawatt factory would be able to save around $2M in Silver costs alone.

Table 2.7: Possible Savings if Implemented into a GigaWatt Factory

	Silver Cost ($)	Savings with Respect to Cell A ($)
Cell A	$11,105,769.23	$0
Cell B	$10,391,826.92	$713,942.31
Cell C	$9,122,596.15	$1,983,173.08

These designs are not limited to G1 cells, but can expanded into the settling standard of G12. By making a projection about the metalization to area ratio of G1, the silver consumption of G12 can be approximated. the results of the projection can be seen in Table 2.8

Table 2.8: G12 Projection

	Cell A	Cell B	Cell C
Projected Silver Consumption (mg)	123.7	115.8	102.3
Silver Cost (¢)	10.21	9.55	8.44
Metalization Cost Per Watt ($\frac{¢}{W}$)	1.46	1.36	1.21

By scaling the metalization cost per watt of G12 onto a Gigawatt factory in Table 2.9, the benefit of these designs is further cemented. By adopting Cell C's design a

the factory would be able to save approximately $2.5M .

Table 2.9: G12 Projected Savings

[redacted]	Silver Cost ($)	Savings with Respect to Cell A ($)
Cell A	$14,584,351.34	$0
Cell B	$13,646,785.90	$937,565.44
Cell C	$12,058,375.32	$2,525,976.02

CHAPTER 3: PROPOSED METALIZATION PATTERNS ON G12 CELLS

3.1 Introduction

G12 cells have piqued the attention of the photovoltaics community due to their large size as seen in Figure 3.1.

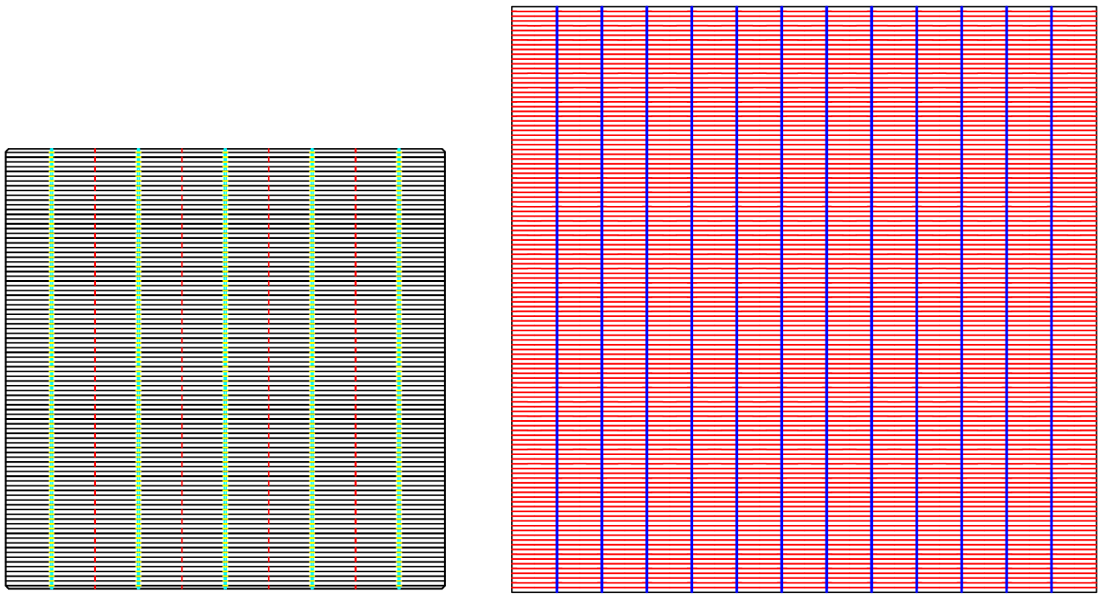

Figure 3.1: G1 vs G12 Cell

Such large area benefits from the shingling of solar cells into modules as seen in Figure 3.2. This allows for various smaller cells to be produced while only manufacturing one large cell, making the manufacturing process much more efficient. Furthermore, shingling yields better results than using a single large area cell, because it lowers the I^2R losses by having a lower current per section. This allows for a higher fill factor and efficiency. With that being said, it is the aim of this chapter to address a front grid design which provides a low metalization cost and is suited for shingling technology.

3.2 Experimental Procedure

The experiment begins with the design of the screen on the AutoCAD software. The front grid design was inspired by the works of [12], in which the total shading area due

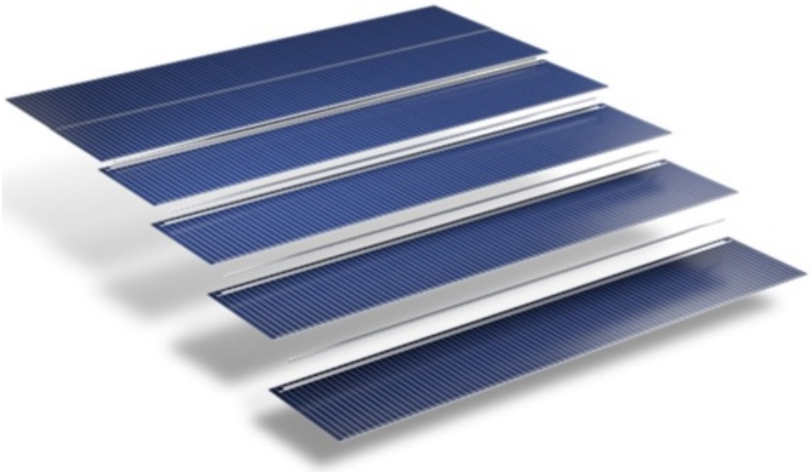

Figure 3.2: Shingled Solar Module [13]

to the busbars was kept constant as the number of busbars increased. Furthermore, the choice of 12BB was based on a prediction from [23] for the optimum number of busbars on G1 cells. The outstanding performance of tapered fingers on G1 cells prompted their adoption into the G12 cell design. The aim of this section is to address the effect of streets, even busbars, and uneven busbars on the characterization parameters and monetary impact of G12 cells. With that in mind a control group composed of G12 cells with no streets, tapered fingers, and 12 busbars will be split into a set of cells with even busbars and uneven busbars. The experimental group has the same attributes as the control group with the addition of streets. The control group is best depicted in Figures 3.3 & 3.5. Similarly, the experimental group is best described in Figures 3.7 & 3.9. Finally, the experimental parameters are summarized in Table 3.1.

Table 3.1: Summary of Experimental Solar Cell Parameters.

Cell Parameter	Cell D	Cell E	Cell F	Cell G
Busbar Design	Even	Uneven	Even	Uneven
Number of Streets	0	0	11	11

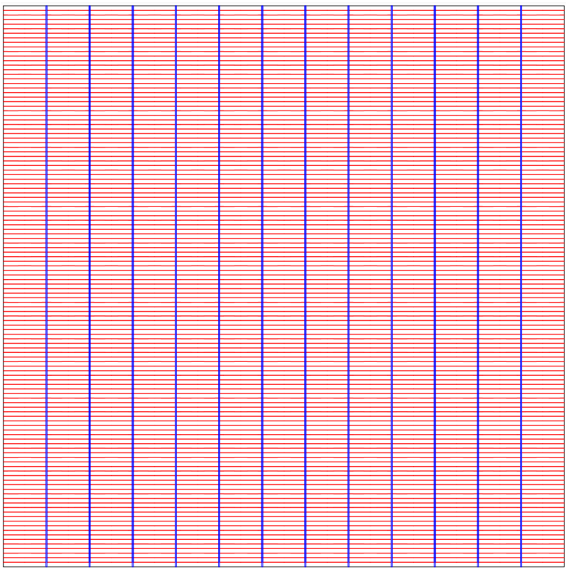

Figure 3.3: Cell D

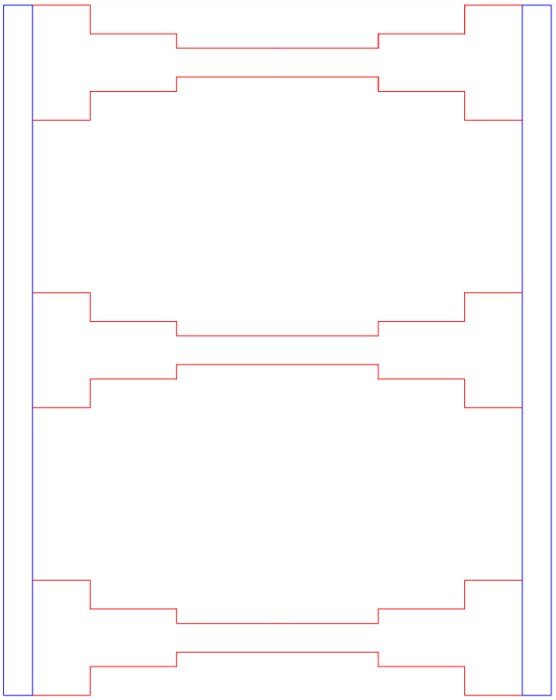

Figure 3.4: Cell D Zoom

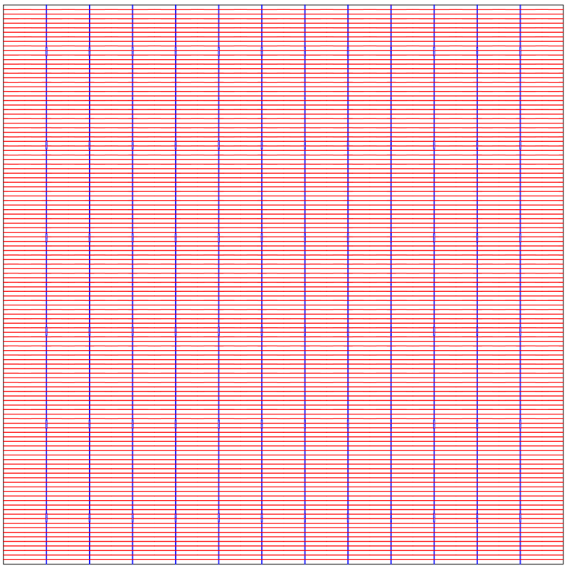

Figure 3.5: Cell E

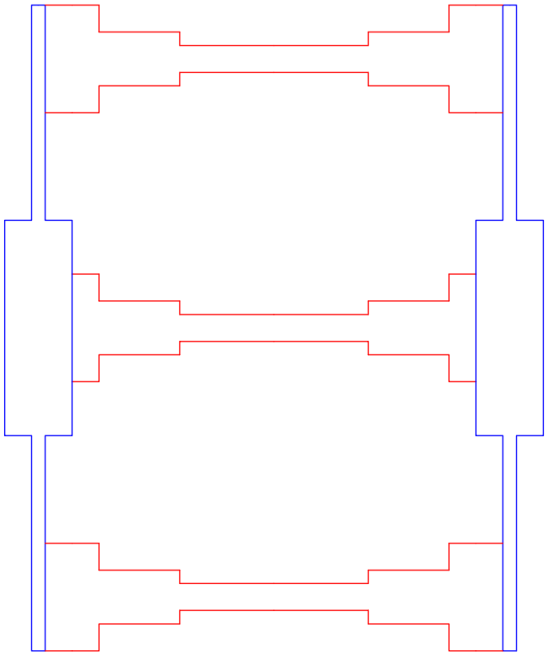

Figure 3.6: Cell E Zoom

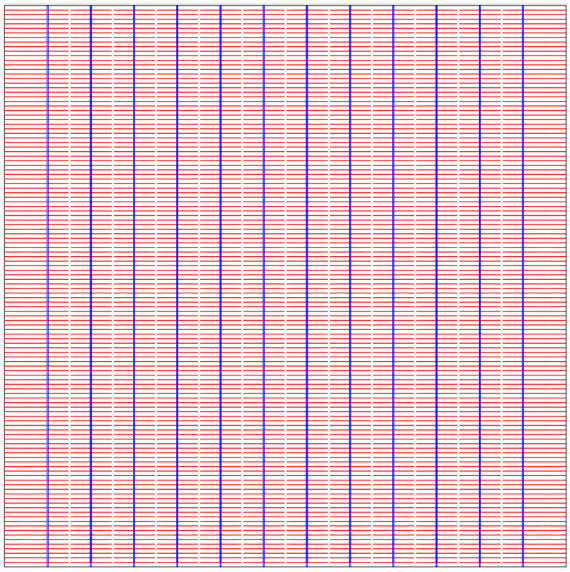

Figure 3.7: Cell F

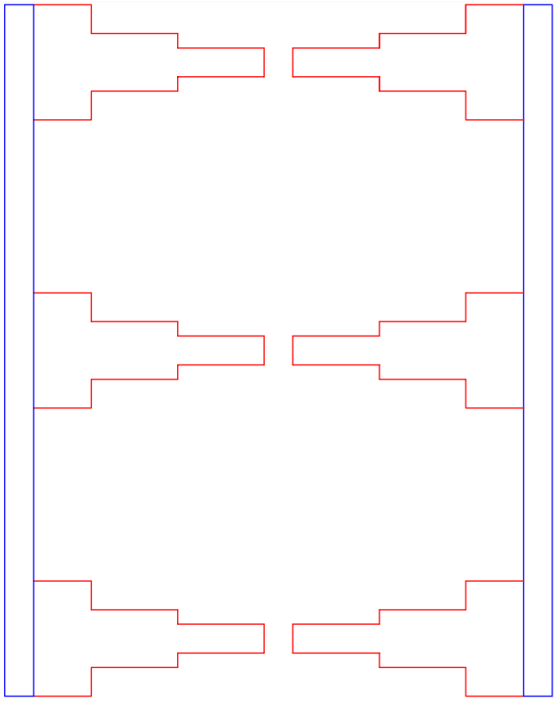

Figure 3.8: Cell F Zoom

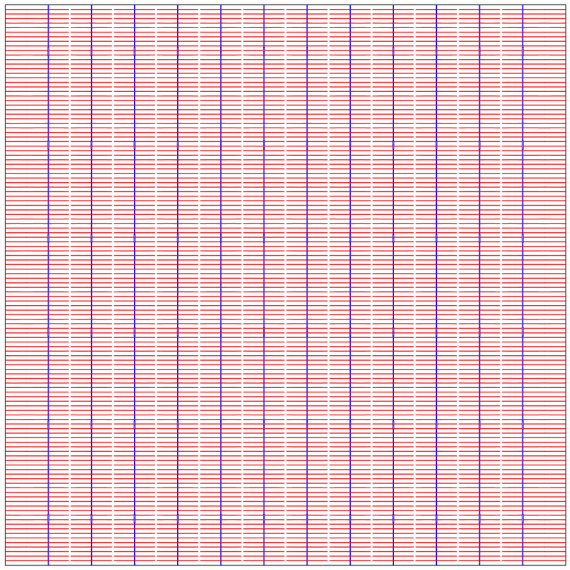

Figure 3.9: Cell G

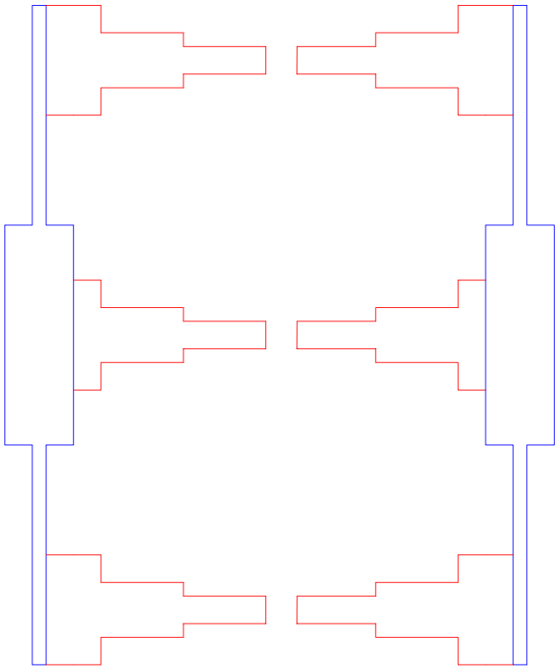

Figure 3.10: Cell G Zoom

3.3 Results

Simulations of the control and experimental group were performed through the cooperation of the grid model mentioned in Section 1.4 of the introduction and PC1D.

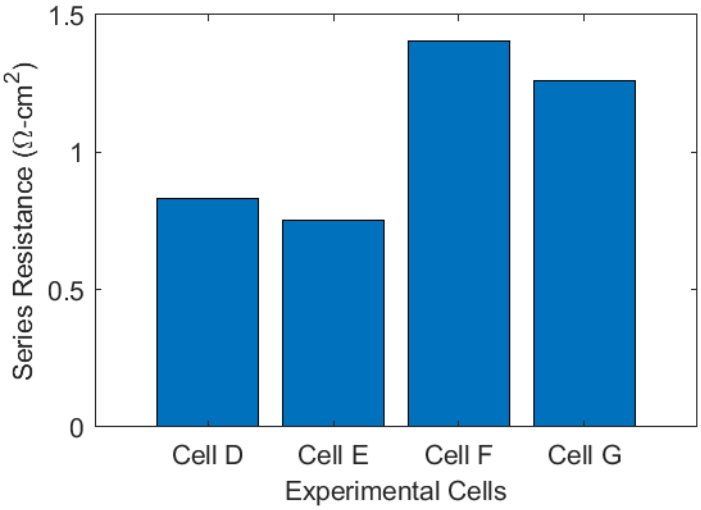

Figure 3.11: Series Resistance Results

As can be seen in Figure 3.11 the series resistance increases with the addition of streets. This is mainly due to the fact the there is less Silver available to facilitate the motion of the charge carriers, increasing the resistance; however, the addition of uneven busbars helps to slightly lower the series resistance.

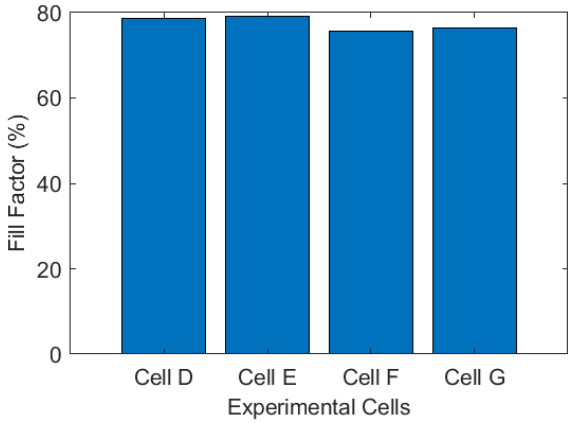

Figure 3.12: Fill Factor Results

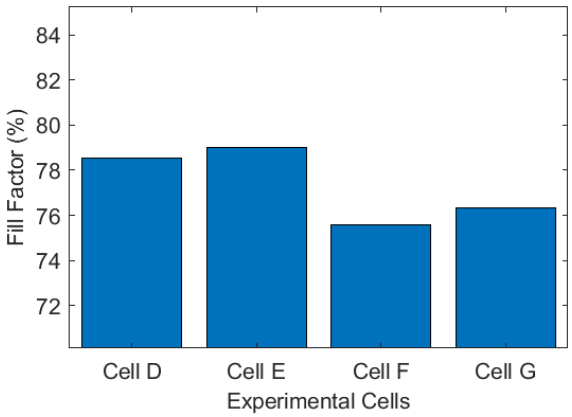

Figure 3.13: Zoom of Fill Factor Results

The high series resistance has a detrimental effect on the fill factor as seen in Figure 3.13 of designs with streets; however, the addition of uneven busbars on Cell G slightly increases the fill factor due a lower series resistance.

The efficiency follows a similar trend to the fill factor shown in Figure 3.14 results.

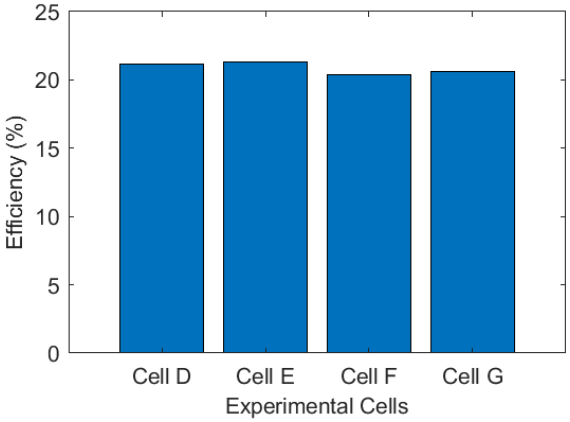

Figure 3.14: Efficiency Results

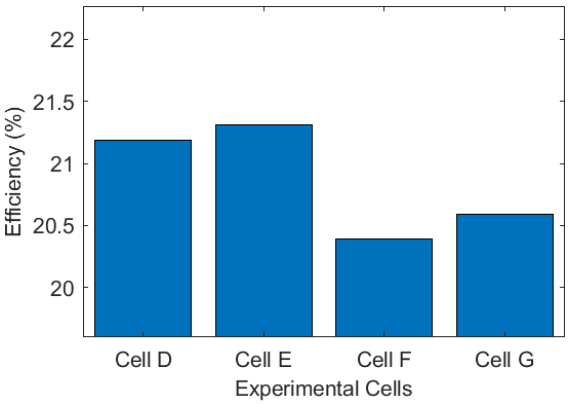

Figure 3.15: Zoom of Efficiency Results

Table 3.2: G12 Projected Silver Consumption

	Cells D & E	Cells F & G
Projected Silver Consumption (mg)	101.6	63.9
Silver Cost (¢)	8.39	5.28
Metalization Cost per Watt ($\frac{¢}{W}$)	1.198	0.754

3.4 Monetary Impact

In order to justify the advantages of the aforementioned designs a similar monetary analysis was made on the G12 designs. This analysis is also based on a projection from the silver consumption of the G1 Cells. Furthermore, since the busbar area was maintained constant for all four designs, the only aspect that changed from a Silver consumption point of view was the streets. Table 3.2 depicts the projected Silver consumption of the new designs.

By scaling the metalization cost per Watt of the designs into a Gigawatt factory environment, the advantages of Cell G's design is solidified. The adoption of this design could potentially save up to $7M in comparison to Cell A's.

Table 3.3: G12 Projected Savings

	Silver Cost ($)	Savings with Respect to Cell A
Cells A	$14,584,351.34	$0
Cells D & E	$11,9800,002.89	$2,604,348.45
Cells F & G	$7,535,801.80	$7,048,549.54

CHAPTER 4: CONCLUSIONS

Cost effectiveness is key to adoptability of solar electricity at a competitive rate with other sources of electricity. Thus, both efficiency and cost should be the major factors for assessing a solar technology as well as the associated processes. It has been shown in this thesis work that, through an innovative front grid the efficiency of the commercial solar cells can be preserved while reducing the production cost. In particular, the innovative front gridline design has shown superior cost savings in the second most expensive layer of a solar cell, the metallization. For the upcoming G12 standardized commercial wafer size, for one GW factory, cost savings of $7M has been identified. This was projected from the experimental results obtained from the G1 commercial wafer size, that showed $2M for the same factory size. It is apparent that once the printing of the front gridline with the innovative screen designs, the efficiency will be at least at par with the conventional grid design in addition to cost savings in the amount of silver consumed.

Further advantage of the innovative design includes the fabrication of the new modules to match the cell efficiency using the shingling design. The ability to produce various cells from a single larger cell is unprecedented, especially for designs such as Cell G's. Typically, when these shingled cells are produced, the dicing saw cuts through the gridlines. This results in higher edge recombination and thus lower efficiency; however, Cell G implemented 11 streets. This means that the cell can be cut into 12 pieces while the dicing saw cuts through the streets and not through the gridlines. This will result in better performance among other advantages.

REFERENCES

[1] J. Donev, "Earth's energy flow," *Energy Education*, Sep 2021.

[2] "Greenhouse effect," *Wikipedia*, Nov 2021.

[3] W. S. School, "The fundamentals of the water cycle active," *The Fundamentals of the Water Cycle*, Jul 2019.

[4] "Photoelectric effect," *Wikipedia*, Dec 2021.

[5] R. Nave, "P-n energy bands," *Biasing of P-N Junctions*.

[6] P. Szaniawski, *From Light To Dark: Electrical Phenomena in Cu (In, Ga) Se2 Solar Cells*. PhD thesis, Acta Universitatis Upsaliensis, 2017.

[7] D. S. Chan and J. C. Phang, "Analytical methods for the extraction of solar-cell single-and double-diode model parameters from iv characteristics," *IEEE Transactions on Electron devices*, vol. 34, no. 2, pp. 286–293, 1987.

[8] "Series resistance," *PVEducation*.

[9] M. Jamadi, F. Merrikh-Bayat, and M. Bigdeli, "Very accurate parameter estimation of single-and double-diode solar cell models using a modified artificial bee colony algorithm," *International Journal of Energy and Environmental Engineering*, vol. 7, no. 1, pp. 13–25, 2016.

[10] "Fill factor," *PVEducation*.

[11] V. Unsur, *Understanding and Developing Fire-Through Dielectric Contacts on Highly Efficient Silicon Solar Cells*. PhD thesis, The University of North Carolina at Charlotte, 2018.

[12] A. Ebong, N. Chen, V. Unsur, A. Chowdhury, and B. Damiani, "Innovative front grid design, four-streets and five-busbars (4s-5bb), for high efficiency industrial al-bsf silicon solar cell," *IEEE Electron Device Letters*, vol. 37, no. 4, pp. 459–462, 2016.

[13] "What are shingled solar panels?," Aug 2020.

[14] A. Ollila, "The greenhouse effect definition," *Physical Science International Journal*, pp. 1–5, 2019.

[15] "Photoelectric effect," *Encyclopaedia Britannica*.

[16] P. Auger, W. S. Read, , W. Shockley, Read, and R. N. Hall, "Types of recombination," *PVEducation*.

[17] "Shunt resistance," *PVEducation*.

[18] W. Shockley and H. J. Queisser, "Detailed balance limit of efficiency of p-n junction solar cells," *Journal of applied physics*, vol. 32, no. 3, pp. 510–519, 1961.

[19] D. Meier, E. Good, R. Garcia, B. Bingham, S. Yamanaka, V. Chandrasekaran, and C. Bucher, "Determining components of series resistance from measurements on a finished cell," in *2006 IEEE 4th World Conference on Photovoltaic Energy Conference*, vol. 2, pp. 1315–1318, IEEE, 2006.

[20] D. L. Meier, V. Chandrasekaran, A. Gupta, V. Yelundur, and A. Rohatgi, "Silver contact grid: inferred contact resistivity and cost minimization in 19% silicon solar cells," *IEEE journal of Photovoltaics*, vol. 3, no. 1, pp. 199–205, 2012.

[21] L. Jiang, W. Zhang, T. Guo, D. Kapp, L. Yan, and L. Wang, "An improved mathematical modeling to simulate metallization screen pattern trend for silicon solar cell," in *2013 IEEE 39th Photovoltaic Specialists Conference (PVSC)*, pp. 2641–2645, IEEE, 2013.

[22] //www.facebook.com/monexpreciousmetals/, "Silver prices today: Live silver spot price: Silver price charts," Mar 2021.

[23] N. Chen, *Understanding and development of cost-effective industrial aluminum back surface field (Al-BSF) silicon solar cells*. PhD thesis, The University of North Carolina at Charlotte, 2015.